Materials Science for Energy Technologies 5 (2022) 125–144

Contents lists available at ScienceDirect

Materials Science for Energy Technologies

journal homepage: www.keaipublishing.com/en/journals/materials-science-for-energy-technologies

Investigation of electronic structure, morphological features, optical, colorimetric, and supercapacitor electrode properties of $CoWO_4$ crystals

Y.L. Oliveira [a], A.F. Gouveia [b], M.J.S. Costa [a], F.H.P. Lopes [c], J.C. Sczancoski [d], E. Longo [d], G.E. Luz. Jr. [c], R.S. Santos [c], L.S. Cavalcante [a,c,*]

[a] Programa de Pós-Graduação em Ciência dos Materiais-PPGCM, Universidade Federal do Piauí, 64049-550 Teresina, PI, Brazil
[b] Universitat Jaume I (UJI), Department of Physical and Analytical Chemistry, Castellón de la Plana 12071, Spain
[c] PPGQ-GERATEC, Universidade Estadual do Piauí, Rua: João Cabral, N. 2231, P.O. Box 381, 64002-150 Teresina PI, Brazil
[d] CDMF-UFSCar, Universidade Federal de São Carlos, P.O. Box 676, 13565-905 São Carlos, SP, Brazil

ARTICLE INFO

Article history:
Received 25 October 2021
Revised 21 December 2021
Accepted 28 December 2021
Available online 12 January 2022

Keywords:
$CoWO_4$ crystals
Rietveld refinement
Band gap
Colorimetry
Capacitance

ABSTRACT

Cobalt tungstate ($CoWO_4$) crystals were synthesized by the co-precipitation (CP) and polymeric precursor (PP) methods with posterior heat treatment at 800 °C for 4 h. The electronic structure, morphological features, optical, colorimetric, and supercapacitive properties were investigated in detail. X-ray diffraction, Rietveld refinement data, micro-Raman spectra, and Fourier transform-infrared spectra proved the crystallization of both $CoWO_4$ materials with a wolframite-type monoclinic structure. Rietveld refinement data were employed as input data to simulate all clusters found in this crystalline structure as well as electron density maps. These results indicated the existence of distortions in both octahedral [CoO_6] and [WO_6] clusters, yielding an inhomogeneous charge distribution in the monoclinic lattice. Field emission scanning electron microscopy and transmission electron microscopy techniques show the presence of asymmetrical $CoWO_4$ crystals. The ultraviolet–visible diffuse reflectance spectroscopy revealed optical band energy values of 2.84 and 2.89 eV for $CoWO_4$ crystals prepared by the CP and PP methods, respectively. Colorimetric results indicated that the $CoWO_4$ crystals have a desirable feature for the development of blue inorganic pigments. The experimental specific capacitance measurements of $CoWO_4$ crystals as an electrode (CP and PP) were 192.5 Fg^{-1} and 249.1 Fg^{-1} at 40 mV s^{-1} and 5 mV s^{-1} in an electrode with 0.4 mg and 0.8 mg of electroactive materials in 1 M Na_2SO_4 solution, respectively.

1. Introduction

The cobalt tungstate ($CoWO_4$) crystals can be found in small quantities as a result of the burning of coal mine dumps in the mineral form, presenting gray, bluish-gray, and greenish-gray colors [1]. This mineral, also known as "*Krasnoselskite*", has been explored at Krasnoselskaya mines in Krasnogorsk, Chelyabinsk basin, Ural Mountains in Russia [2,3]. According to the literature [4], $CoWO_4$ crystals are not recognized as a natural mineral by the International Mineralogical Association (IMA) [5,6]. These crystals are oxides belonging to the wolframite family [7] with a general formula (AWO_4) (A = Mn^{2+}, Fe^{2+}, Co^{2+}, Ni^{2+}, and Zn^{2+}), space group ($P2/c$), symmetry point group (C_{2h}^4), two molecular formula units per unit cell (Z = 2) and n° 13 in the international crystallography table [8–12]. Among the transition metals belonging to the fourth period of the periodic table (from d^5 to d^{10}), only the tungstate cooper ($CuWO_4$) does not present a wolframite-type monoclinic structure [13]. In particular, the $CuWO_4$ crystals with d^9 electronic configuration exhibits a strong Jahn-Teller distortion in octahedral [CuO_6] clusters gives rise to a d-orbital splitting, in which the degeneracy of σ-antibonding orbitals is broken, which decreases its symmetry and modifies its lattice to the triclinic structure at room temperature [14–17].

According to the literature, the $CoWO_4$ crystals can be obtained via traditional routes performed at high temperatures (>900 °C) and long processing times (>4h) as conventional solid-state reaction, oxide-mixture, crystal growth flux and reduction/oxidation reactions [18–27]. In addition, other more elaborate synthesis methods have been employed to prepare the $CoWO_4$ (microcrystals, nanocrystals and films), including proteic sol–gel green [28], solid-state metahetic [29], polymeric precursor [30], facile refluxing-calcination [31,32], molten salt [33,34], conventional hydrothermal [35–38], microwave hydrothermal [39,40], precipi-

* Corresponding author at: Programa de Pós-Graduação em Ciência dos Materiais-PPGCM, Universidade Federal do Piauí, 64049-550 Teresina, PI, Brazil.
E-mail address: laeciosc@gmail.com (L.S. Cavalcante).

https://doi.org/10.1016/j.mset.2021.12.006
2589-2991/

tation or co-precipitation [41–45], sonochemical [46,47], alcohol-thermal [48], spray pyrolysis [49], and pulsed laser deposition [50].

In relation to the electronic properties of $CoWO_4$ crystals, different studies have demonstrated that this tungstate is a good candidate for technological applications in high-density capacitors [51–55], solid-electrolyte galvanic cells [56], catalysts for hydrogen evolution reaction [57], magnetic [58–60], electric transport [61], microwave dielectric [62], photoluminescence [63], photocatalyst [64,65], electrocatalytic [66], tribological [67], desulfurization [68], sensitive nonenzymatic glucose sensor [69], acetone gas sensing [70], high capacity anode material for lithium-ion batteries [71], and color properties [72].

However, few theoretical studies have been reported in the literature, explained by means of *ab initio* calculations, also known as the first-principles method based on the density-functional theory (DFT) or by means of a full-potential linearized augmented plane wave (FP-LAPW) for resolution of the electronic structure in $CoWO_4$ crystals with the correlation between experimental data and theoretical calculation [73,74], and few investigations have been reported in the literature on their colorimetric properties [72].

Thus, in this paper, $CoWO_4$ crystals were synthesized by two chemical methods (co-precipitation and polymeric precursor) with posterior heat treatment at 800 °C for 4 h. These crystals were characterized by using X-ray diffraction (XRD) patterns, Rietveld refinements, micro-Raman, and Fourier transforms infrared (FT-IR) spectroscopies. The morphology aspects were observed by field emission images scanning electron microscopy (FE–SEM) and transmission electron microscopy (TEM). The optical band gap values of these crystals were obtained from ultraviolet–visible (UV–Vis) diffuse reflectance spectroscopy. Finally, we investigated the colorimetric analyses in a colorimeter in the CIELAB color space and electrochemical behavior using cyclic voltammetry at different scan rates for applications of $CoWO_4$ electrodes as high-density capacitors. Our study on $CoWO_4$ crystals provide a news insight into the colorimetric and electrochemical investigations with the main difference for supercapacitor performance between $CoWO_4$ submicron and microcrystals as electrodes. These results suggest this oxide material as a potential candidate for energy storage in the future.

2. Experimental details

2.1. Synthesis of $CoWO_4$ crystals by the co-precipitation and polymeric precursor methods

Initially, $CoWO_4$ crystals were prepared by the co-precipitation (CP) method, with some modifications in relation to the synthesis method described in [75]. The synthesis of $CoWO_4$ crystals is described as follows: 3.3318 g of sodium tungstate (VI) dihydrate [$Na_2WO_4{\cdot}2H_2O$; 99% purity, Sigma-Aldrich®] and 2.9696 g of cobalt (II) nitrate hexahydrate [$Co(NO_3)_2{\cdot}6H_2O$ 98% purity, Dynamic®] were separately placed in two beakers with a capacity of 500 L and dissolved using a volume of 250 mL for each beaker with deionized water (DI-H_2O). In this solution containing $Co^{2+}_{(aq)}$ and $2NO^{-}_{3(aq)}$ ions was noted the formation of a complex with light red color, commonly detected when the pH of the solution is maintained at 7.5 [76]. This chemical reaction involving Co^{2+} ions and H_2O molecules is able to rapidly produce the hexaaquacobalt(II) complex ion, $[Co(H_2O)_6]^{2+}$, with octahedral symmetry (O_h) [76]. The addition of 1.6 mL of nitric acid [HNO_3; 65% purity, Merck®] to this solution changes the pH to 4.5 due to an increase of the concentration of H_3O^+ and NO_3^- ions. The chemical equilibrium is shifted in the reaction, destabilizing the $[Co(H_2O)_6]^{2+}$ complex and releasing Co^{2+} ions in the reaction medium. After this pH modification, 200 mL was added to the second solution containing $Na^{+}_{(aq)}$ and $WO^{2-}_{4(aq)}$ ions, which was maintained under constant stirring at 75 °C for 2 h. After this process, the formation of a purple suspension containing **$CoWO_{4(s)}$** precipitates was observed. The chemical reactions involved in this synthesis are summarized in equations (1–4):

$$Co(NO_3)_2.6H_2O_{(s)} \overset{n.H_2O}{\rightarrow} [Co(H_2O)_6]^{2+} + 2NO^{-}_{3(aq)} \quad (1)$$

$$[Co(H_2O)_6]^{2+} + 2NO^{-}_{3(aq)} + 6HNO_3 \overset{pH=4.5}{\rightarrow} 1Co^{2+}_{(aq)} + 6H_3O^{+} + 8NO^{-}_{3(aq)} \quad (2)$$

$$Na_2WO_4.2H_2O_{(s)} \overset{n.H_2O}{\rightarrow} 2Na^{+}_{(aq)} + 1WO^{2-}_{4(aq)} + 2H_2O \quad (3)$$

$$1\mathbf{Co^{2+}_{(aq)}} + 6H_3O^{+} + 8NO^{-}_{3(aq)} + 2Na^{+}_{(aq)} + 1\mathbf{WO^{2-}_{4(aq)}} + 2H_2O \overset{75ÂºC/2h}{\rightarrow} \mathbf{CoWO_{4(s)}} + 2Na^{+}_{(aq)} + 6H_3O^{+} + 8NO^{-}_{3(aq)} + 2H_2O \quad (4)$$

The above experimental procedure was performed with great accuracy and reproducibility of data to obtain amorphous **$CoWO_{4(s)}$** precipitates. The precipitates were separated from the liquid phase via centrifugation (9,000 rpm for 10 min) by using DI-H_2O and ethanol (ten times) to remove the by-products of the reaction. In the sequence, the amorphous precipitates were dried at 65 °C for 10 h in a conventional furnace, deagglomerated and placed in a porcelain crucible. Such precipitates were heat treated at 800 °C for 4 h, maintaining a heating rate of 1 °C/min.

$CoWO_4$ crystals were also prepared by the polymeric precursor (PP) method [77]. This synthetic experimental methodology is a modified sol–gel method, which is based on the complexation of metal alkoxides and the esterification/polymerization reaction [78]. Some modification in this synthesis method has been successfully used to obtain nanocrystalline $CoWO_4$ powders when calcined at temperatures from 500 °C to 800 °C [79]. To obtain the crystals, a tungsten metal citrate (*Cit-W*) at pH = 7 was initially prepared by using DI-H_2O as a solvent, and citric acid [$C_6H_8O_7$; 99% purity, Sigma-Aldrich®] as a complexing agent to tungstic acid [H_2WO_4; 99% purity, Sigma-Aldrich®]. After homogenization, cobalt (II) nitrate hexahydrate [$Co(NO_3)_2{\cdot}6H_2O$, 99.9% purity, Sigma-Aldrich®], in which the octahedral $[Co(H_2O)_6]^{2+}$ complex is employed as lattice modifier to tungsten citrate. The *Cit-W* with bivalent cations was stirred at 90 °C for 2 h, forming a homogeneous red solution. Ammonium hydroxide (NH_4OH) was used to adjust the pH at around 7. This solution was polymerized with the addition of ethylene glycol [$C_2H_6O_2$; 99.5% purity, Dynamic®] as polyalcohol. After reaction at a temperature of approximately 90 °C, a polyester and water were formed. The citric acid/metal molar ratio was maintained at 3:1 and 60:40 for citric acid/ethylene glycol to promote citrate polymerization. The polymerized solution was heated until the water evaporated and a polymeric resin formed. The resin was heated at 350 °C for 4 h by using a heating rate of 10 °C/min, forming black amorphous powders. The precursor powders were deagglomerated with mortar and pestle, and heat treated at 800 °C for 4 h by using a heating rate of 1 °C/min. The monophasic $CoWO_4$ crystal (blue color) is found only at high temperatures (≥600 °C) [80].

2.2. Experimental characterizations

$CoWO_4$ crystals were structurally characterized by XRD on a LabX XRD-6000 diffractometer (Shimadzu®, Japan) with Cu-Kα radiation (λ = 1.5406 Å). XRD patterns were collected over 2θ ranging from 10° to 75° with a scanning rate of 2°/min. For Rietveld

refinements, XRD patterns were collected over 2θ ranging from 10° to 110° with a scanning rate and step size of 1°/min and 0.02°, respectively. Micro-Raman spectra were acquired on a Raman Senterra scattering microscope (Bruker Optik, Germany) at 532 nm. These spectra were recorded at room temperature in the region from 85 cm^{-1} to 1,050 cm^{-1}. The incident laser beam power on the sample was mantained at 6 mW, with 250 scans of spectral scanning, a step of 0.5 cm^{-1} and spectral resolution of 4 cm^{-1}. Infrared (IR) spectroscopy was performed to identify the functional groups in the precursors employed in the synthesis of the crystals. FT-IR spectra were obtained on a spectrophotometer (PerkinElmer®, FT-IR Spectrum 100) in the region from 400 to 1,200 cm^{-1}, with a spectral resolution of 4 cm^{-1}. The morphological features were examined by using a FE-SEM from (JEOL®, Japan) in JSM-IT300 model operated at 15 kV, and with a transmission electron microscopy (TEM), from (JEOL®, Japan) in JEM-2100 model with working voltage of 120 kV. The shape, average size and diffraction plane of $CoWO_4$ crystals were determined using the high resolution (HR)-TEM. Optical analyzes were performed in a UV–Vis spectrophotometer (Shimadzu®, Japan) in 2600 model. The optical band gap of the samples was recorded in diffuse reflectance mode in UV–Vis region by using barium sulfate ($BaSO_4$) as the standard. The color of the crystals was acquired on a portable digital colorimeter with 8 mm caliber (FRU®, WR-10QC model) with photodiode array sensor at CIE 10° standard observer, light source D65, luminosity (L*) measuring range 0–100, and through the color difference formula: ΔE *a *b at color space CIELAB defined by the International Commission on Illumination (CIE) in 1976 [81,82].

2.3. Electrochemical capacitance measurements

$CoWO_4$ films (as electrodes) were prepared by using 150 mg of crystalline $CoWO_4$ (CP and PP)/deagglomerated with mortar and pestle, dispersed in acetone (5 mL) and ethylene glycol (5 mL). These $CoWO_4$ suspensions were homogenized in an ultrasonic bath (CPX 1800 Branson) for 30 min, and then, maintained at 50 °C for 2 h under constant stirring. $CoWO_4$ suspensions were deposited to obtain films on a fluorine-doped tin oxide (FTO) coated glass substrate with surface resistivity ~7 Ω/sq by the drop casting method and limited geometric area of 1 cm^2. The deposition of $CoWO_4$ films was performed by adding 40 μL of the suspension on the FTO glass. After evaporation at 55 °C for 3 h, the $CoWO_4$ electrodes were heat tread at 500 °C for 2 h with heating rate at 1 °C/min. The mass of $CoWO_4$ crystals deposited post-heat-treatment were 0.4 mg for $CoWO_4$ film prepared by CP method and 0.8 mg for $CoWO_4$ film prepared by PP method. Electrochemical performances were evaluated by using cyclic voltammetry (CV) curves in an Autolab PGSTAT302N Metrohm potentiostat/galvanostat (Metrohm) at room temperature and the NOVA 1.7 software was employed for data acquisition. All experiments were achieved in a conventional three-electrode cell. $CoWO_4$ was used as working electrode, platinum (Pt) wire and Ag/AgCl electrode in luggin capillary were used as counter electrode and reference electrode, respectively. CV measurements were obtained in different potential window from 0.0 to 0.4, 0.6, 0.8, and 1.0 V, then unique potential window was analyzed different scan rates from 5 to 100 mV s^{-1} in a 1.0 mol L^{-1} Na_2SO_4 aqueous solution (pH ~ 7.0).

3. Results and discussion

3.1. XRD patterns analysis

Fig. 1(a,b) shows the XRD patterns of $CoWO_4$ crystals prepared by the CP and PP methods, both heat-treated at 800 °C for 4 h.

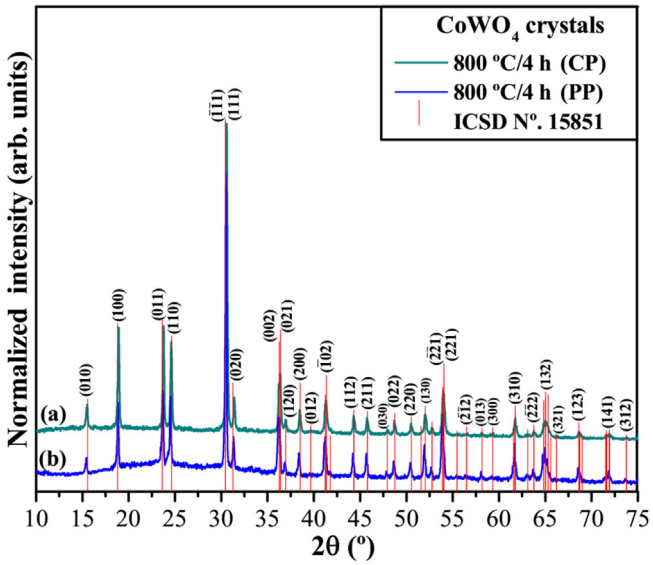

Fig. 1. XRD patterns of $CoWO_4$ crystals synthesized by the (a) CP and (b) PP methods. The red vertical lines (|) indicate the position and relative intensity of XRD patterns of $CoWO_4$ phase reported in ICSD with CIF file No. 15851.

According to the literature [83], XRD patterns can be employed to prove the degree of structural order–disorder at long-range or the periodicity of crystalline lattice of $CoWO_4$ crystals. As can be seen in Fig. 1(a,b), the normalized XRD patterns of $CoWO_4$ crystals exhibited diffraction peaks indexed to the wolframite-type monoclinic structure [84,85] and Inorganic Crystal Structure Database (ICSD) with the crystallographic information file (CIF) Nº. 15851 reported by Weitzel at 1976 [86]. Moreover, the diffraction peaks were slightly broader for $CoWO_4$ crystals prepared by the CP in relation to than verified by the PP method. This particular behavior can be explained by the fact that the crystallite size decreases from bulk to nanoscale dimensions [87]. The Debye–Scherrer equation (5) was employed as shown below [88]:

$$D = \frac{k.\lambda}{\beta.cos\theta} \quad (5)$$

This equation simply and quantitatively describes the broadening of a peak at a particular diffraction angle (θ), as it relates the crystalline domain size (D) to the width of the peak at half of its height (β). The Scherrer constant, k, is typically considered to be 0.94 is a good approximation, but can vary with the morphology of the crystalline domains [89]. The X-ray wavelength (λ) is a constant that depends on the type of X-rays used. Each peak can be evaluated independently and should produce a consistent crystalline domain size so long as the sample can be roughly approximated as uniform, spherical particles [90]. Therefore, the Debye–Scherrer equation (5) can be used to obtain the XRD crystallite size of $CoWO_4$ crystals. The domain sizes calculated were ~41.34 nm for $CoWO_4$ crystals obtained by the CP method, and ~46.58 nm for $CoWO_4$ crystals synthesized by the PP method. Although $CoWO_4$ crystals prepared by the CP method appear to exhibit wide-range XRD peaks when calculating the Full Width at Half Maximum (FWHM) for the (0 1 0) plane located at around 15.5° presents D value larger than $CoWO_4$ crystals prepared by the PP method. Note that in the Debye–Scherrer equation (5), the diffraction angle is in radians (not degrees) and corresponds to θ and not 2θ, as is typically plotted in an XRD pattern. Also, note that crystalline domain size does not necessarily correspond to particle size, as particles can be polycrystalline, containing multiple crystalline domains. When the crystalline domain size calculated by the

Debye–Scherrer equation (5) matches the average diameter of particles determined by more precise methods (e.g., FE–SEM images, or TEM images), it suggests that the particles prepared by the CP method are formed by polycrystalline nanocrystals. For further clarification, we employed the Rietveld refinement analysis to explain this difference between the degrees of long-range order–disorder and different distortions in octahedral [CoO_6]/[WO_6] clusters in the monoclinic lattice.

3.2. Rietveld refinement analysis

The Rietveld refinement method is based on the construction of diffraction patterns calculated in relation to the structural model employed as a crystallographic standard [91,92]. This structural refinement uses the patterns calculated with a fit of the adjustment in relation to finding pattern data to provide the structural parameters of the sample and the profile diffraction [92]. In this paper, the Rietveld refinement method was applied to adjust the best lattice parameters of the unit cell, structural factors such as atomic positions, and atomic isotropic displacement parameters (U_{iso}) due to the different synthesis methods used to obtain the $CoWO_4$ crystals. In these analyses, the refined parameters were the shift lattice constants, background, scale factor, profile half-width parameters (u, v, w), isotropic thermal parameters, lattice parameters, and atomic positions. The background was corrected using a three (P1, P2, and P3) polynomial functions of the first kind [93]. The peak profile function was modeled by using a convolution of the Thompson-Cox-Hastings pseudo-Voigt function [94] to effectively improving our Rietveld refinement data.

Fig. 2(a,b) illustrate the Rietveld refinement plots for the observed patterns versus calculated patterns of $CoWO_4$ crystals prepared by the CP and PP methods, respectively.

As can be seen in Fig. 2(a,b), our XRD patterns at Rietveld routine were adjusted to the (experimentally) observed pattern diffraction profile, providing the structural parameters of the desired material and its (calculated) diffraction profile. In this study, the Rietveld refinement method was applied to estimate the atomic positions, lattice parameters, and unit cell volume of the $CoWO_4$ crystals. This refinement method allows for finding peculiar structural features of $CoWO_4$ crystals produced by each type of synthesis. The Rietveld refinement was performed using the *ReX* software version 0.9.2 [95], using the ICSD of CIF file No. 15851 [86], which presents consistent crystallographic patterns in good agreement with studies previously reported in the literature [96]. The single $CoWO_4$ crystals have a wolframite-type monoclinic structure, presenting a space group ($P2/c$), symmetry point group (C_{2h}^4), and two molecular formula units per unit cell ($Z = 2$). The structural refinement confirmed the presence of $CoWO_4$ crystals with phase pure without any secondary or deleterious phases. In general, slight differences in the intensity scale were identified between experimental and calculated XRD patterns, as described by the line ($Y_{Obs} - Y_{Calc}$), and as illustrated in Fig. 2(a,b). However, $CoWO_4$ crystals prepared by the CP present a major difference at the line ($Y_{Obs} - Y_{Calc}$). The experimentally obtained data from Rietveld refinement are displayed in Tables 1(a,b), respectively:

The data presented in Tables 1(a,b) for fit parameters (R_p, R_{wp}, R_{exp}, χ^2, and *GoF*) were obtained consistently within Rietveld's criteria. After repeated Rietveld refinement cycles and fine-tuning of structural parameters to find the lowest and best possible values for the two $CoWO_4$ crystals, which confirm the quality, reproducibility, and reliability of these data. In general, some few variations in the atomic (x, y, z) positions for O1, O2 atoms, and (y) atomics positions for Co and W atoms were observed, while the Co and W atoms occupying special (x, z) atomics positions into the monoclinic lattice, remain fixed during all the structural refinement. Subsequently, the lattice parameters and atomic positions obtained from the Rietveld refinement analysis will be used to start the optimization of the calculated electronic structure by the DFT method in a further paper..

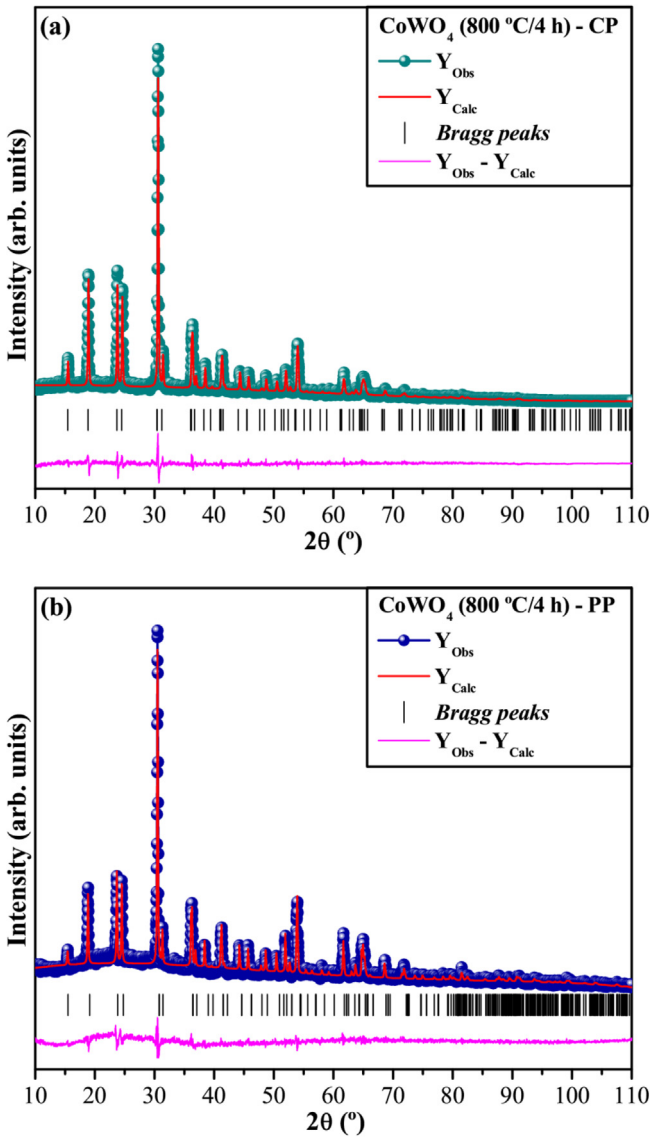

Fig. 2. Rietveld refinement plots of $CoWO_4$ crystals synthesized by the (a) CP and (b) PP methods, respectively.

3.3. Clusters coordination and charges map electron density analysis

Fig. 3(a,b) illustrate a schematic representation of the monoclinic structure with the lattice parameters, internal angle (β) of the ($1 \times 1 \times 1$) unit cell, and [O–Co–O]/[O–W–O] bonds of $CoWO_4$ crystals synthesized by the CP and PP methods, respectively.

The wolframite-type monoclinic structure for $CoWO_4$ crystals was modeled by using the visualization system for electronic and structural analysis (VESTA) software version 3.5.7 for Windows 10®-64 bits [97,98]. The lattice parameters and atomic positions obtained from Rietveld refinement data are listed in Tables 1(a, b). As can be noted in Fig. 3(a,b), the distorted octahedral [CoO_6] and [WO_6] clusters are formed by different types of octahedron polyhedrons with 6 vertices, 8 faces, and 12 edges [99]. Moreover, we have verified that both crystals have the internal angle

Table 1a
Rietveld refinement data of $CoWO_4$ crystals synthesized by the CP method.

Atoms	*Wyckoff*	*Site*	*x*	*y*	*z*	U_{iso}
Co	2*f*	2	0.5	0.669812	0.25	0.044309
W	2*e*	2	0.0	0.182346	0.25	0.051526
O1	4*g*	1	0.218883	0.116066	0.954182	0.059304
O2	4*g*	1	0.273348	0.381309	0.385495	0.001803

a = 4.6713(3) Å, *b* = 5.685(2) Å, *c* = 4.95156(4) Å, V = 131.500(9)Å^3; α = γ = 90°, β = 89.99297(4)°; R_p(%) = 10.2007.
R_{exp}(%) = 8.4985, R_{wp}(%) = 12.7579, χ^2 = 2.253594, *GoF* = 1.5012; ρ = 7.75 g/cm^3, and μ/ρ = 164.98 cm^2/g.

Table 1b
Rietveld refinement data of $CoWO_4$ crystals synthesized by the PP method.

Atoms	*Wyckoff*	*Site*	*x*	*y*	*z*	U_{iso}
Co	2*f*	2	0.5	0.666125	0.25	0.099467
W	2*e*	2	0.0	0.180954	0.25	0.106288
O1	4*g*	1	0.099286	0.099286	0.929666	0.099319
O2	4*g*	1	0.248704	0.35799	0.397271	0.065079

a = 4.70117(8) Å, *b* = 5.72087(4) Å, *c* = 4.98201(9) Å, V = 133.990(6)Å^3; α = γ = 90°, β = 90.02595(4)°; R_p(%) = 7.7364.
R_{exp}(%) = 9.9954, R_{wp}(%) = 11.6727, χ^2 = 1.363768, *GoF* = 1.167805; ρ = 7.60 g/cm^3, and μ/ρ = 169.27 cm^2/g.

(β ≠ 90°), while the $CoWO_4$ crystals prepared by the PP method have a longer length in the *b* lattice parameter and unit cell volume (Tables 1(a,b)), indicating a more anisotropic behavior than $CoWO_4$ crystals prepared by the CP method [100]. It is possible to note that these $CoWO_4$ crystals present some variations in both [O–Co–O] and [O–W–O] bond angles and lengths. This characteristic result implies in distortions in the octahedral [CoO_6] and [WO_6] clusters with distinct degrees of order–disorder in the lattice. Finally, as can be observed in Fig. 3(a,b), $CoWO_4$ crystals prepared by the CP method exhibit more distortions in their chemical bonds than those prepared by the PP method.

Fig. 4(a–f) display the 2D isolines of electron density models into the (1 × 1 × 1) unit cell on the (1 1 1), (0 1 0), and (1 2 1) planes for $CoWO_4$ crystals prepared by the CP and PP methods.

The 2D isolines of electron density models were calculated by using the Fourier transform structure factor from the structure parameters and atomic scattering factors of free atoms obtained from Rietveld refinement data of $CoWO_4$ crystals prepared by the CP and PP methods, respectively. These data were used in the VESTA software version 3.5.7 [97,98] to obtain the 2D isolines of electron density models with a high resolution from 0.015 to 0.020 Å. These figures show different and sensible color scales on each specific plane, which indicate zones with high and low electron densities. In Fig. 4(a), the blue color regions are related to the absence of electronic charge, yellow color regions are ascribed to the medium electron densities, while the red color areas exhibit a high electronic density in the (1 1 1) plane. Moreover, it is possible to verify the presence of non-homogeneous electronic charge distributions near the [O–Co–O] bonds related to an atomic displacement, indicating the existence of large distortions between Co and O atoms (Fig. 4(a)). We have observed two W atoms, one Co atom, and three O atoms in the (0 1 0) plane due to the presence of distortions in the octahedral [WO_6] clusters (Fig. 4(b)). For $CoWO_4$ crystals prepared by the CP method, it was observed that the Co and W atoms are able to share the same O1 and O2 atoms in the (1 2 1) plane. This behavior is explained by the differences in the distances of [O–Co–O] and [O–W–O] bonds due to the presence of two different octahedral [CoO_6]/[WO_6] clusters in crystals with type-wolframite monoclinic structures (Fig. 4(c)). Fig. 4(d–f) show the 2D isolines of the electrons density maps for $CoWO_4$ crystals prepared by the PP method. In the (1 1 1) plane, also it observed a non-homogeneous distribution of electronic charges between the [O–Co–O] bonds, presenting smaller distortions than those presented by the CP method. In the (0 1 0) plane, the same distortions on the octahedral [WO_6] clusters and presence of electronic interaction or charges proximity between the O1 and W atoms were observed, as shown in Fig. 4(e). Finally, in the (1 2 1) plane, it was observed that the Co and W atoms share the same O1 and O2 atoms, with a higher electron charge density on the Co atoms, as shown in Fig. 4(f). Moreover, it was noted that the O2 atom exhibited a minor electronic charge density on the (1 2 1) plane for $CoWO_4$ crystals prepared by the PP method. These results corroborate the cluster's coordination model illustrated earlier in Fig. 3 (a,b).

3.4. Micro-Raman spectra analysis

The tungstates crystals with a wolframite-type monoclinic structure present a total of (3 *N* = 36 degrees of freedom), as described by means of standard group theory analysis, space group (*P*2/*c*), symmetry point group (C_{2h}^4), two molecular formula units per unit cell (Z = 2) and n° 13 in the international crystallography table of these oxides [101–103]. Therefore, we have the presence of *N* = 12 atoms within the monoclinic unit cell, as illustrated previously in Fig. 3(a,b). In our case, $CoWO_4$ crystals have 36 distinct vibration modes (Raman) and [IR], as indicated in equation (6) [103,104]:

$$\Gamma_{\{(\text{Raman})+[\text{Infrared}]\}} = \{(8A_g + 10B_g) + [8A_u + 10B_u]\} \quad (6)$$

where the A_g and B_g, are Raman-active vibrational modes, while A_u and B_u are active vibrational modes in the infrared spectra. The A and B modes are nondegenerate. The subscripts "$_g$" and "$_u$" indicate the parity under inversion in centrosymmetric $CoWO_4$ crystals. Therefore, only 18 active vibrational modes are expected in the Raman spectra of these $CoWO_4$ crystals, as represented by reduced equation (7) below [105]:

$$\Gamma_{(\text{Raman})} = (8A_g + 10B_g) \quad (7)$$

According to the recent literature [106,107], structural refinement data obtained employing Rietveld method and group theory calculations. $CoWO_4$ crystals exhibited a wolframite-type monoclinic structure, which is composed and formed only by distorted octahedral [CoO_6] and [WO_6] clusters. Therefore, these crystals have a group symmetry (O_h) and symmetry site (C_2). The micro-Raman spectra of the $CoWO_4$ crystals can be classified into two types of groups (external and internal vibrational modes). The external vibrational modes are related to the lattice phonons, which correspond to the motion of distorted octahedral [CoO_6]

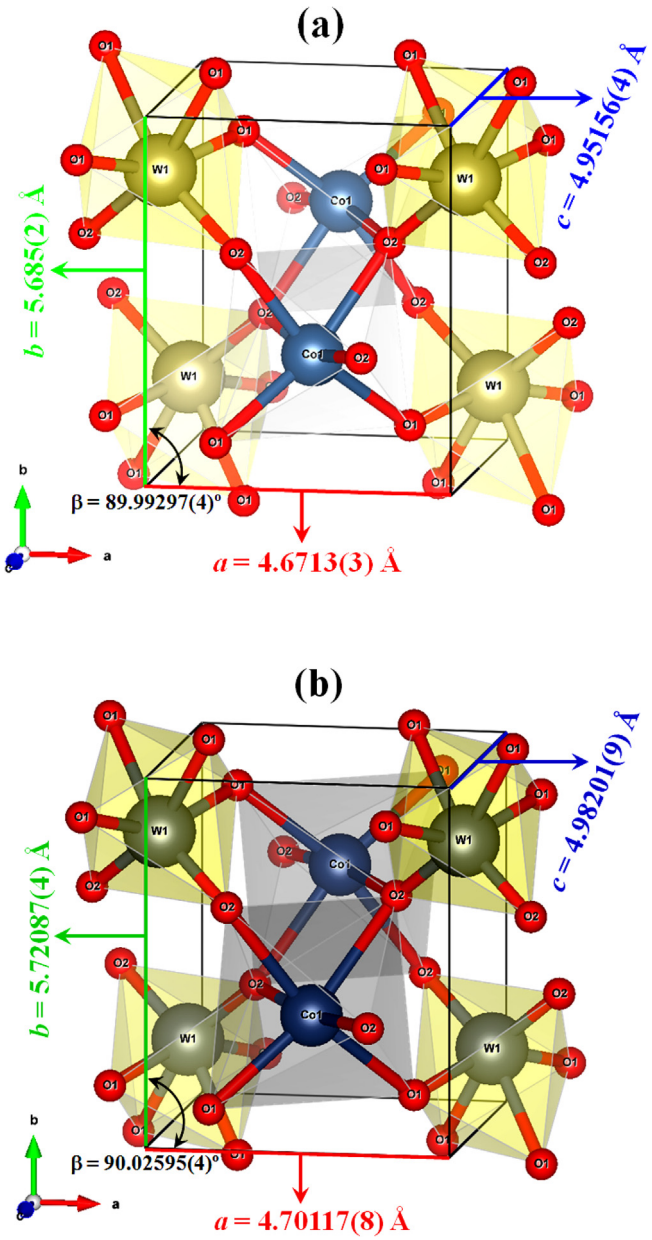

Fig. 3. (a,b): Schematic representation of (1 × 1 × 1) unit cells for $CoWO_4$ crystals synthesized by the CP and PP methods, respectively. The distorted octahedral [CoO_6] and [WO_6] clusters show the internal (β angles), lattice parameters, [O–Co–O] and [O–W–O] bonds, respectively.

clusters in the monoclinic unit cell. The internal vibrational modes are ascribed to vibrations of distorted octahedral [WO_6] clusters, assuming a center of mass of the steady state. The distorted octahedral [WO_6] clusters have group symmetry (O_h), where these vibrations are composed of 6 internal vibrational modes ($4A_g$ and $2B_g$). The other external vibrational modes ($4A_g$ and $8B_g$) in the Raman spectra are related to different optical modes, and stretching and bending vibrations types such as: symmetric, antisymmetric, scissoring, twisting, rocking, wagging, and transverse at short-range of bonds in between two distorted octahedral [$_5$OW–O–WO_5] clusters and interconnected distorted octahedral [$_5$OW–O–CoO_5–O–WO_5] clusters [108].

Fig. 5(a,b) displays the micro-Raman spectra for $CoWO_4$ crystals prepared by the CP and PP methods, respectively.

As can be observed in Fig. 5(a,b), we can identify the presence of 18 Raman active vibrational modes between 85 and 1,050 cm^{-1} for $CoWO_4$ crystals prepared by two methods. However, the $CoWO_4$ crystals prepared by means of the PP method exhibited active-Raman vibrational modes vibrational sharper and better defined. This behavior can be explained by means of Raman spectroscopy has proved its potential as a powerful vibrational spectroscopic technique for a fundamental and molecular-level characterization of the vibration of chemical bonds, thus providing access to the extended structure of crystalline solids (via phonons) but also the short-range structure of amorphous materials [109]. The main active-Raman (A_g) vibrational mode and intense peak located at around 881–884 cm^{-1} is ascribed to the symmetric stretching of bonds ν_{sym}[←O2 ← W → O_5 →] of distorted octahedral [WO_6] clurters, as shown in inset Fig. 5(a,b). Moreover, 2 active-Raman ($1A_g$ and $1B_g$) vibrational modes at approximately (802–803 cm^{-1}) is related to the anti-symmetric stretching of $\nu_{antisym}$[-↖O2↖W↙O_5↙] bonds and at around (703–711 cm^{-1}) is ascribed to the symmetric stretching of ν_{sym}[←$_5$OW–O–WO_5 →] bonds between distorted octahedral [WO_6]–[WO_6] clusters in good agreement with the literature [103,108] (inset Fig. 5(a,b)), while the active-Raman ($1B_g$) vibrational mode with low intensity at around 190–191 cm^{-1} is ascribed to the transverse optical T́[↙Co↙O↗–O_5↗] (inset Fig. 5(a,b)). Therefore, all the active-Raman vibrational modes, which were identified on the Raman peaks are corresponding to a wolframite-type monoclinic structure. The experimental positions of 18 active-Raman vibrational modes were identified as (● for $CoWO_4$ crystals prepared by CP method) and (■ for $CoWO_4$ crystals prepared by PP method). Their relative position for all active-Raman vibrational modes were compared with those Raman-active modes reported in the literature and are listed in Table 2.

As can be noted in Table 2, there is a good agreement between the Raman-active vibrational modes for our $CoWO_4$ crystals prepared by CP and PP method, some works reported in the literature synthesized experimentally and theoretically calculated by Vienna *ab initio* package [101–103]. Some small variations in the typical positions of the Raman vibrational modes can be caused by the different preparation methods, average crystal size, distortions in (O–Co–O)/(O–W–O) bonds, interaction forces involving octahedral [WO_6]–[CoO_6]–[WO_6] clusters and/or different degrees of order–disorder structural in the monoclinic lattice.

As previously described in the text, the Raman and IR spectra displayed 36 different vibrational modes, which were presented in equation (6). These modes, only some of them are active in the infrared spectrum. Therefore, only 18 vibrational modes are expected in the IR spectra of $CoWO_4$ crystals, as represented in equation (8) below [108]:

$$\Gamma_{[\text{Infrared}]} = [8A_u + 10B_u] \quad (8)$$

However, 3 modes ($1A_u$ and $2B_u$) are only acoustic vibrations and can not be detected in the infrared spectrum. Therefore, in equation (8) should be reduced and can be better represented by the following equation (9) [103,108]:

$$\Gamma_{[\text{Infrared}]} = [7A_u + 8B_u] \quad (9)$$

In general, the IR spectroscopy can be divided into three regions (near, mid and far), and these transition metal oxides as our $CoWO_4$ crystals have many vibrational modes in the far infrared region. Therefore, all 15 infrared-active vibrational modes only can be detectable with a better FT-IR spectrophotometer in the far region, cesium iodide pellets as background, or high-performance optional transit Platinum ATR accessory. Unfortunately, our FT-IR equipment is limited. Moreover, this technique

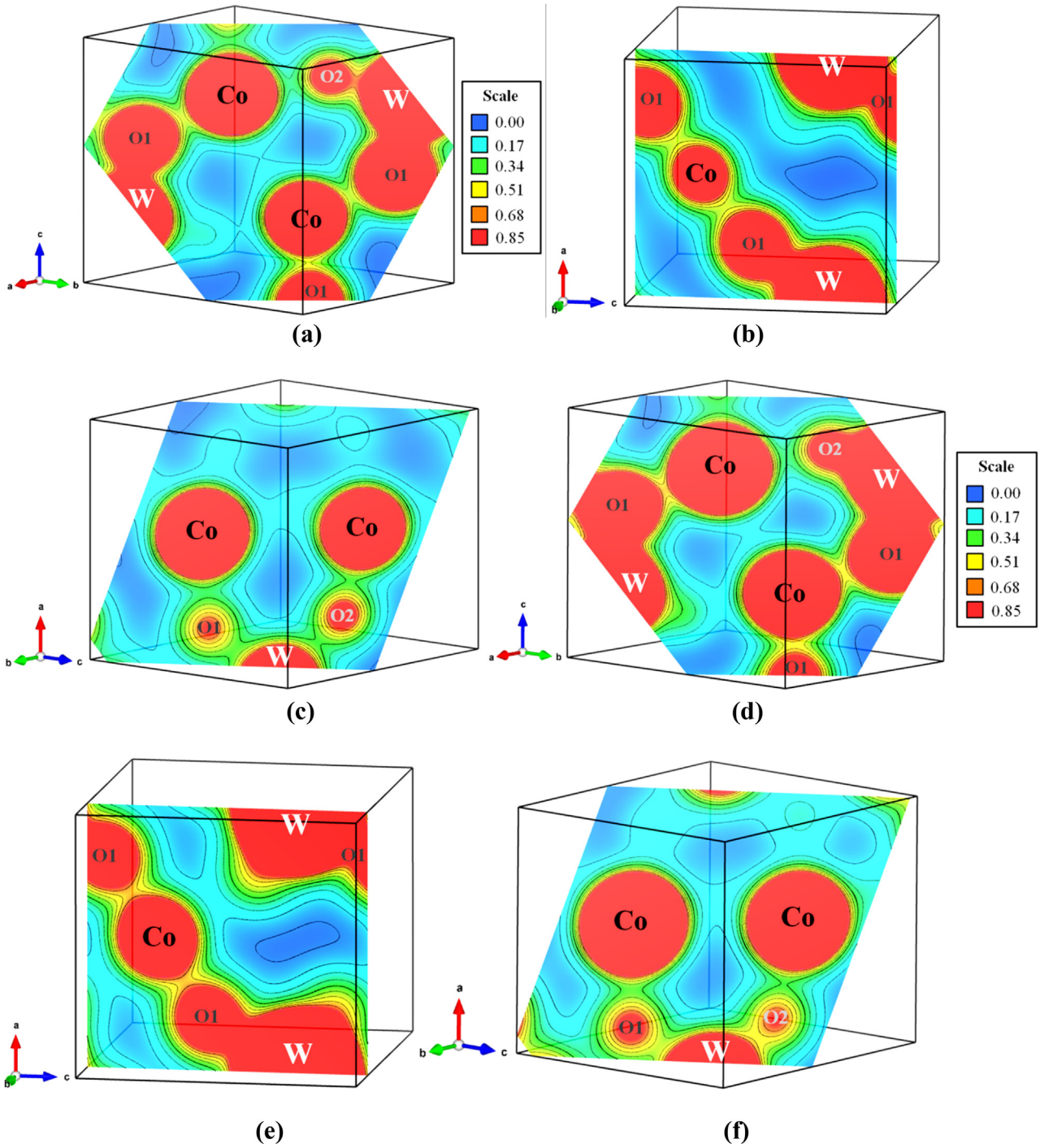

Fig. 4. Electron density maps in (a,d) (111), (b,e) (010), and (c,f) (121) planes of $CoWO_4$ crystals synthesized by the CP and PP methods, respectively.

can elucidate the type difference of IR-active vibrational modes between the Co and O atoms, the W and O atoms, and their inter-atomic bonds in $CoWO_4$ crystals [110].

Fig. 6(a,b) display the FT-IR spectra of $CoWO_4$ crystals synthesized by the CP and PP methods, respectively.

As can be observed in Fig. 6(a,b) for both $CoWO_4$ crystals, the dynamic force between atoms is associated with the highest energy modes can be understood based on the main atomic shifts. In our FT-IR spectra of $CoWO_4$ crystals prepared by the CP and PP methods, it was only possible to detect 7 IR-active vibrational modes from 400 to 1,200 cm^{-1} were identified as (● for $CoWO_4$ crystals prepared by CP method) and (■ for $CoWO_4$ crystals prepared by PP method), which are related to the $4A_u$ and $3B_u$ modes, as shown in Fig. 6(a,b). The $1A_u$ mode located at around 863–864 cm^{-1} is ascribed to the symmetric stretching vibrations of $\nu_{sym}[\leftarrow O2 \leftarrow W \rightarrow O_5 \rightarrow]$ presents in distorted octahedral $[WO_6]$ clusters. Also observed was a smaller IR-band at 821–830 cm^{-1}, which be related to the optical $1B_u$ mode at the zone center reported by Kalinko *et al.* [104] or anti-symmetric stretching vibrations of $\nu_{antisym}[\nwarrow O2 \nwarrow W \swarrow O_5 \swarrow]$ bonds in distorted octahedral $[WO_6]$ clusters. Another band of low intensity at 692–690 cm^{-1} is referred to anti-symmetric stretching vibrations of $\nu_{antisym}[\nwarrow_5 O \nwarrow W \swarrow O \swarrow WO_5 \swarrow]$ bonds in distorted octahedral $[WO_6]$ clusters (inset Fig. 6(a,b)) [10,105]. Also observed was a

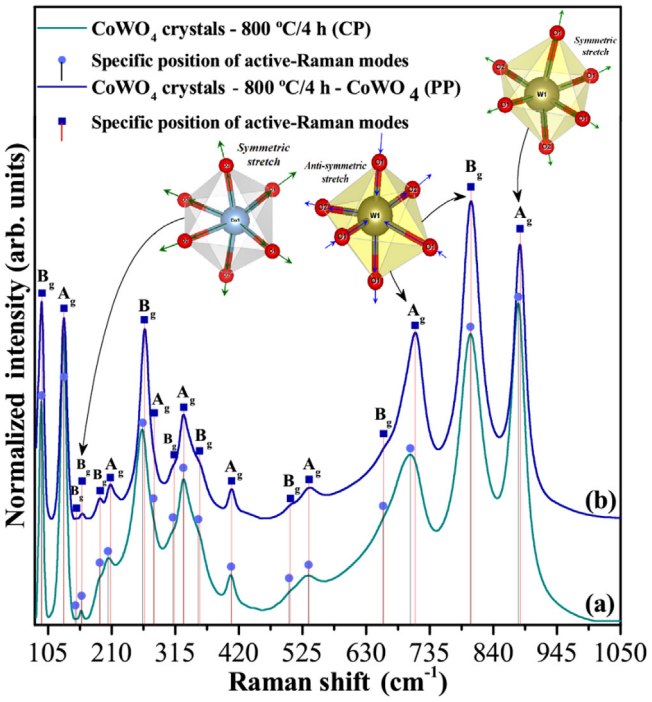

Fig. 5. (a,b): Micro-Raman spectra for $CoWO_4$ crystals synthesized by the (a) CP and (b) PP methods. Inset in Fig. 5(a,b) show the distorted octahedral [CoO_6] clusters with symmetric stretch for B_g mode, distorted octahedral [WO_6] clusters with anti-symmetric stretch for A_g and B_g modes, and distorted octahedral [WO_6] clusters with symmetric stretch for A_g mode, respectively.

shoulder at 641–613 cm^{-1} ($1B_u$ mode) is attributed to optical modes for $\nu_{antisym}[\nwarrow_5O\nwarrow W\swarrow O\swarrow WO_5\swarrow]$ bonds in distorted octahedral [WO_6] clusters [108]. Moreover, $1A_u$ mode located at 528–532 cm^{-1}, which be related to the optical $1B_u$ mode for anti-symmetric stretching vibrations and scissoring vibrations of $\nu_{antisym}[\nwarrow_5O\nwarrow W\swarrow O\swarrow WO_5\swarrow]$ + $\delta_{scis}[\nwarrow O2\nwarrow W\nearrow O_5\nearrow]$ bonds in octahedral [WO_6] clusters, $1B_u$ mode in 467–469 cm^{-1} ascribe to anti-symmetric stretching vibrations of $\delta_{antisym}[\nwarrow_5O\nwarrow W\swarrow O\swarrow WO_5\swarrow]$ bonds and $1A_u$ mode in 434–435 cm^{-1} is the assignment to anti-symmetric stretching and twisting modes ascribed to $\delta_{antisym}[\nwarrow_5O\nwarrow W\swarrow O\swarrow W\swarrow O_5]$ bonds + $\tau[\swarrow O2\swarrow W\nearrow O_5\nearrow]$ bonds in distorted octahedral [WO_6] clusters [108]. A comparison between the respective positions of IR-active vibrational modes of $CoWO_4$ crystals obtained in our study with others published in the literature [10,103–105] are shown in Table 3:

As shown in Table 3, the IR-active modes found in our $CoWO_4$ crystals obtained by CP and PP methods indicate good agreement between the wavenumbers of infrared-active modes reported in the literature.

3.5. Morphological features of $CoWO_4$ crystals

3.5.1. FE-SEM images analysis and average crystal size

The morphological aspects such as shape, dispersion, aggregation, and average crystal size of $CoWO_4$ crystals obtained by the CP and PP methods were observed by FE-SEM images, as shown in Fig. 7(a–f).

As can be seen in FE-SEM image at low magnification at 23,000× in Fig. 7(a), the $CoWO_4$ crystals obtained by the CP method exhibit several quasi-spherical-like crystals and some irregular ellipse-like crystals. We attribute that our synthesis condition in the CP method is responsible for promoting the growth of this particles. Furthermore, we propose that these $CoWO_4$ crystals are formed by self-assembly of several nanocrystals, as shown in FE-SEM image at high magnification at 45,000× (Fig. 7(b)). This growth process is dominant for a random and spontaneous aggregation of small $CoWO_4$ crystals to form larger ellipse-like $CoWO_4$ crystals and it is thermodynamically driven because larger crystals are more energetically favored than smaller crystals [111]. In recent studies [112–115], $CoWO_4$ nanoparticles can be easily obtained at the nanoscale. However, few papers show $CoWO_4$ crys-

Table 2
Comparative data for respective positions of Raman-active modes of $CoWO_4$ crystals reported in the literature with those obtained in the present study.

Lattice mode symmetry (O_h^7)	Synthesis method		FGT + MF	THEO	IPSOPH	MF	CP	PP
	T (°C)	*Raman-active mode assignment*	1000	–	300	1000	800	800
	t (h)		–	–	–	–	4	4
Raman active vibrational modes	B_g	$\acute{T}[\swarrow W\swarrow O\nearrow-O_5\nearrow]$	88	99	–	93.9	94	95
	A_g	$\acute{T}[\swarrow W\swarrow O\nearrow-O_5\nearrow]$	125	140	–	133.7	131	131
	B_g	$\acute{T}[\swarrow Co\swarrow O\nearrow-O_5\nearrow]$+ $\acute{T}[\swarrow W\swarrow O\nearrow-O_5\nearrow]$	154	168	–	161.6	150	152
	B_g	$\acute{T}[\swarrow Co\swarrow O\nearrow-O_5\nearrow]$+ $\acute{T}[\swarrow W\swarrow O\nearrow-O_5\nearrow]$	185	192	–	164.2	160	161
	B_g	$\acute{T}[\swarrow Co\swarrow O\nearrow-O_5\nearrow]$	199	193	–	188.4	190	191
	A_g	$\acute{T}[\swarrow Co\swarrow O\nearrow-O_5\nearrow]$	–	237	–	211.1	204	208
	B_g	$\tau[\swarrow O2\swarrow W\nearrow O_5\nearrow]$	271	292	–	271.7	261	264
	A_g	$\rho[\nwarrow O2\nwarrow W\nearrow O_5\nearrow]$+ $\acute{T}[\swarrow Co\swarrow O\nearrow-O_5\nearrow]$	–	299	–	280.4	279	280
	B_g	$\omega[\swarrow O2\swarrow W\nwarrow O_5\nwarrow]$	315	317	–	308.9	311	313
	A_g	$\delta_{scis}[\nwarrow O2\nwarrow W\nearrow O_5\nearrow]$ + $\nu_{sym}[\leftarrow_5OW–O–WO_5\rightarrow]$	332	361	–	338.3	328	329
	B_g	$\delta_{sym}[\leftarrow_5OW–O–WO_5\rightarrow]$ + $\rho[\leftarrow O2\leftarrow W\rightarrow O_5\rightarrow]$	–	379	–	355.1	353	355
	A_g	$\nu_{sym}[\leftarrow_5OW–O–WO_5\rightarrow]$	403	407	–	406.6	407	408
	B_g	$\nu_{sym}[\leftarrow_5OW–O–WO_5\rightarrow]$	496	510	–	508.9	503	505
	A_g	$\delta_{sym}[\leftarrow_5OW–O–WO_5\rightarrow]$	530	551	–	540.3	535	536
	B_g	$\nu_{sym}[\leftarrow_5OW–O–WO_5\rightarrow]$	657	646	–	656.8	658	659
	A_g	$\nu_{sym}[\leftarrow_5OW–O–WO_5\rightarrow]$	686	692	693	691.9	703	711
	B_g	$\nu_{antisym}[\nwarrow O2\nwarrow W\swarrow O_5\swarrow]$	765	781	–	770.8	802	803
	A_g	$\nu_{sym}[\leftarrow O2\leftarrow W\rightarrow O_5\rightarrow]$	881	874	890.3	884.9	881	884
Ref.	–		[101]	[101]	[102]	[103]	[✠]	[✠]

T = Temperature; *t* = time; FGT = Flux Growth Technique; MF = Melted Flux; IPS = Inorganic Polymer Syntheses; CP = Co-Precipitation; PP = Polymeric Precursor; THE = Theoretical by DFT in the Vienna *ab initio* simulation package; sym = Symmetric; antisym = Anti-symmetric; scis = Scissoring; τ = Twisting; *ρ* = Rocking; ω = Wagging; $\acute{T}$ = Transverse; Raman-active vibrational modes = (cm^{-1}), *Ref.* = References and ✠= This Work.

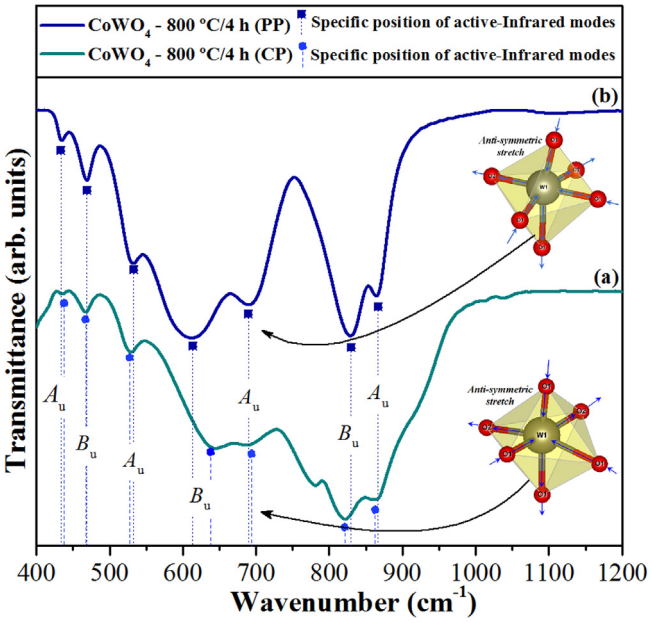

Fig. 6. FT-IR spectra for $CoWO_4$ crystals synthesized by the (a) CP and (b) PP methods. Inset in Fig. 6(a,b) distorted octahedral [WO_6] clusters with antisymmetric stretching vibration for A_u and B_u modes, respectively.

tals on the micrometer scale [102,107] until the present year. This behavior is possibly due to the good stability of $[Co(H_2O)_6]^{2+}$ cobalt cationic complex in aqueous media, which decreases the electronic attraction with $[WO_4^{2-}]$ tungsten anionic complex, decreasing reaction kinetics, growth rate, and the average size of $CoWO_4$ crystals. As can be seen in Fig. 7(c,d), we can observe the presence of several rod-like $CoWO_4$ microcrystals and some quasi-spherical-like crystals. Therefore, $CoWO_4$ crystals prepared by the PP method present preferentially more anisotropic than isotropic growth. The heat treatment performed at 800 °C for 2 h induced a decomposition process of residual organic compounds and promoted the appearance of pores, which were slowly reduced by the microparticles' growth, forming large aggregated regions with irregular shapes [116]. Moreover, the thermal energy favors the diffusion mechanism, leading to the microparticles accumulating into a more dense mass (Fig. 7(d)), resulting in necking between the grains. This growth mechanism occurs through the grain boundary motion due to a reduction in the total grain boundary surface energy [117]. In general, the crystalline oxides prepared by the PP method exhibit irregular morphologies, non-uniform particle size distribution, and a very agglomerated nature. To compare the shape and average crystal size of $CoWO_4$ crystals obtained by the CP and PP methods, we counted 160 crystals with good contour and quality in several FE-SEM images. The Shapiro–Wilk (W) normality test was employed to verify that data are normally distributed [118]. In all cases, the counting of crystal sizes is well described by a log-normal distribution according to equation (10) below:

$$y = y_0 + \frac{A}{\sqrt{2\pi}wx} e^{\frac{-\left[\ln\frac{x}{x_c}\right]^2}{2w^2}} \quad (10)$$

where y_0 is the first value in the y-axis, A is the amplitude, w is the width, π is a constant, and x_c is the center value of the distribution curve in the x-axis. The average size distribution for $CoWO_4$ crystals obtained by the CP method were counts and estimated in the range from 150 to 375 nm; thus, these crystals are in submicrometer scale from 100 to 1000 nm (Fig. 7(e)). Moreover, these $CoWO_4$ crystals exhibit irregular sphere-shaped with major percentual for average crystals size at around 31% referent to 275 nm. Therefore, according to the literature [119], these $CoWO_4$ crystals are not nanometric, since the nanocrystals present an average size distribution from 1 to 100 nm, when belonging to nanoscale, with significant and intriguing optical properties [120]. Moreover, the average particle size distribution of $CoWO_4$ crystals obtained by the PP method has been estimated in the range from 600 nm to 1.5 μm (Fig. 7(f)). Moreover, these $CoWO_4$ crystals exhibit a rod-like shape and also some quasi-spherical-like with major percentual for average crystals size at around 36% referent to 900 nm. However, a considerable percentage (%) relative at around 38.75% of the $CoWO_4$ crystals prepared by the PP method is between 1.0 and 1.5 μm, which are due to the presence of $CoWO_4$ microcrystals, while the 61.25% are ascribed to other smaller $CoWO_4$ crystals with an average size between 600 and 900 nm at the sub-micrometer scale. In both cases, the average crystal size was estimated using the GNU Image Manipulation Program (GIMP 2.99.6) version for Windows 10®-64 bits [121]. Finally, all our statistical data obtained through the counting of particle sizes using FE-SEM images were well-described by the log-normal distribution.

3.5.2. TEM and HR-TEM images analysis

Fig. 8(a–h) display TEM and HR-TEM images of $CoWO_4$ crystals prepared by the CP method (a–d) and PP method (e–h) both heat treated at 800 °C for 4 h, respectively.

Through the analysis of TEM and HR-TEM images is possible to confirm the size and shape of $CoWO_4$ crystals prepared by the CP and PP methods. Fig. 8(a–c) show the presence of some $CoWO_4$ nanocrystals prepared by the CP method with aggregated and irregular nature. However, HR-TEM images were possible to confirm the pristine crystal and monoclinic structure of $CoWO_4$ phase. HR-TEM image displayed in Fig. 8(d) shows the presence of some

Table 3
Comparative data for respective positions of IR-active modes of $CoWO_4$ crystals reported in the literature with those obtained in the present study.

Lattice mode Symmetry (O_h^7)	Synthesis method		SSR	MF	LCAO	SCP	CP	PP
Infrared active vibrational modes	*T* (°C)	*Infrared-active mode assignment*	1100	1000	–	800	800	800
	t (h)		2	–	–	2	4	4
	A_u	$\delta_{antisym}[\nwarrow_5O\nwarrow W\swarrow O\swarrow W\swarrow O_5]$+ $\tau[\swarrow O2\swarrow W\nearrow O_5\nearrow]$	445.57	433	434	430	434	435
	B_u	$\delta_{antisym}[\nwarrow_5O\nwarrow W\swarrow O\swarrow WO_5\swarrow]$	470.78	463	444	–	467	469
	A_u	$\nu_{antisym}[\nwarrow_5O\nwarrow W\swarrow O\swarrow WO_5\swarrow]$ + $\delta_{scis}[\nwarrow O2\nwarrow W\nearrow O_5\nearrow]$	–	510	505	–	528	532
	B_u	$\nu_{antisym}[\nwarrow_5O\nwarrow W\swarrow O\swarrow WO_5\swarrow]$	531.63	538	535	–	641	613
	A_u	$\nu_{antisym}[\nwarrow_5O\nwarrow W\swarrow O\swarrow WO_5\swarrow]$	685.30	625	651	605	692	690
	B_u	$\nu_{antisym}[\nwarrow O2\nwarrow W\swarrow O_5\swarrow]$	–	759	742	–	821	830
	A_u	$\nu_{sym}[\leftarrow O2 \leftarrow W \rightarrow O_5 \rightarrow]$	855.11	841	854	850	863	864
Ref.	–	–	[10]	[103]	[104]	[105]	✠	✠

T = Temperature; *t* = Time SSR = Solid state reaction; MF = Melted Flux; LCAO = Linear combination of atomic orbital (LCAO) calculations; SCP = Simple chemical precipitation; CP = Co-Precipitation; PP = Polymeric precursor; sym = Symmetric; antisym = Anti-symmetric; scis = Scissoring; τ = Twisting; ρ = Rocking; ω = Wagging; Ť = Transverse; Infrared active vibrational modes = (cm^{-1}); *Ref.* = References and ✠= This Work.

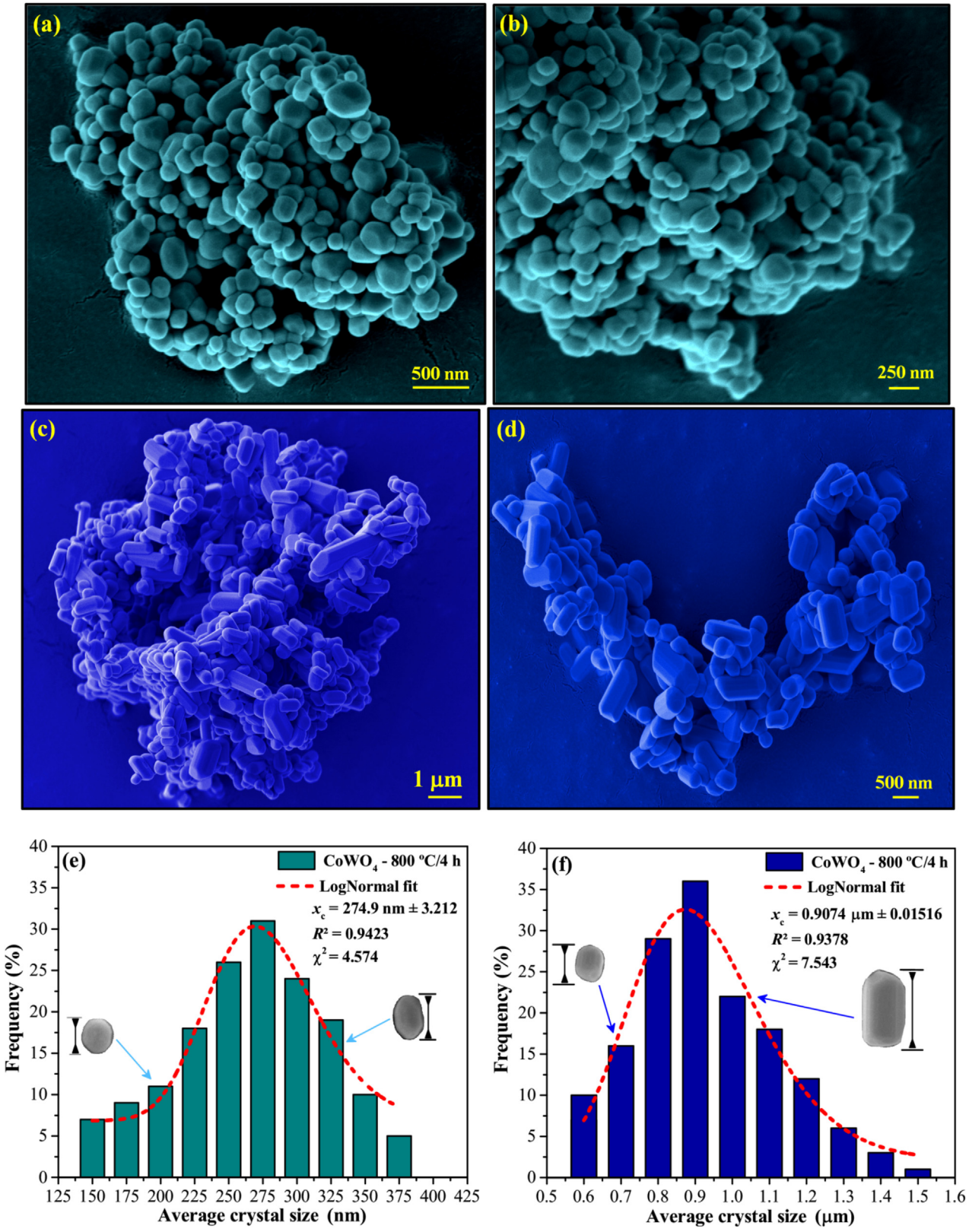

Fig. 7. FE-SEM images at low and high magnification of $CoWO_4$ crystals synthesized by the (a,b) CP and (c,d) PP methods, and (e,f) average crystal size distribution for $CoWO_4$ crystals obtained by the CP and PP methods, respectively.

$CoWO_4$ crystals with diameters of approximately 200 nm. HR-TEM image displayed in Fig. 8(d) shows an interplanar distance for these nanocrystals estimated at around 3.72 Å, which correspond to (0 1 1) crystallographic plane of $CoWO_4$ monoclinic phase (edge of a selected small quasi-spherical $CoWO_4$ crystal). Fig. 8(e–g) illustrate the presence of $CoWO_4$ crystals prepared by the CP method, presenting also an aggregate feature with some rod-like shape more observed than quasi-spherical-like crystals. Therefore,

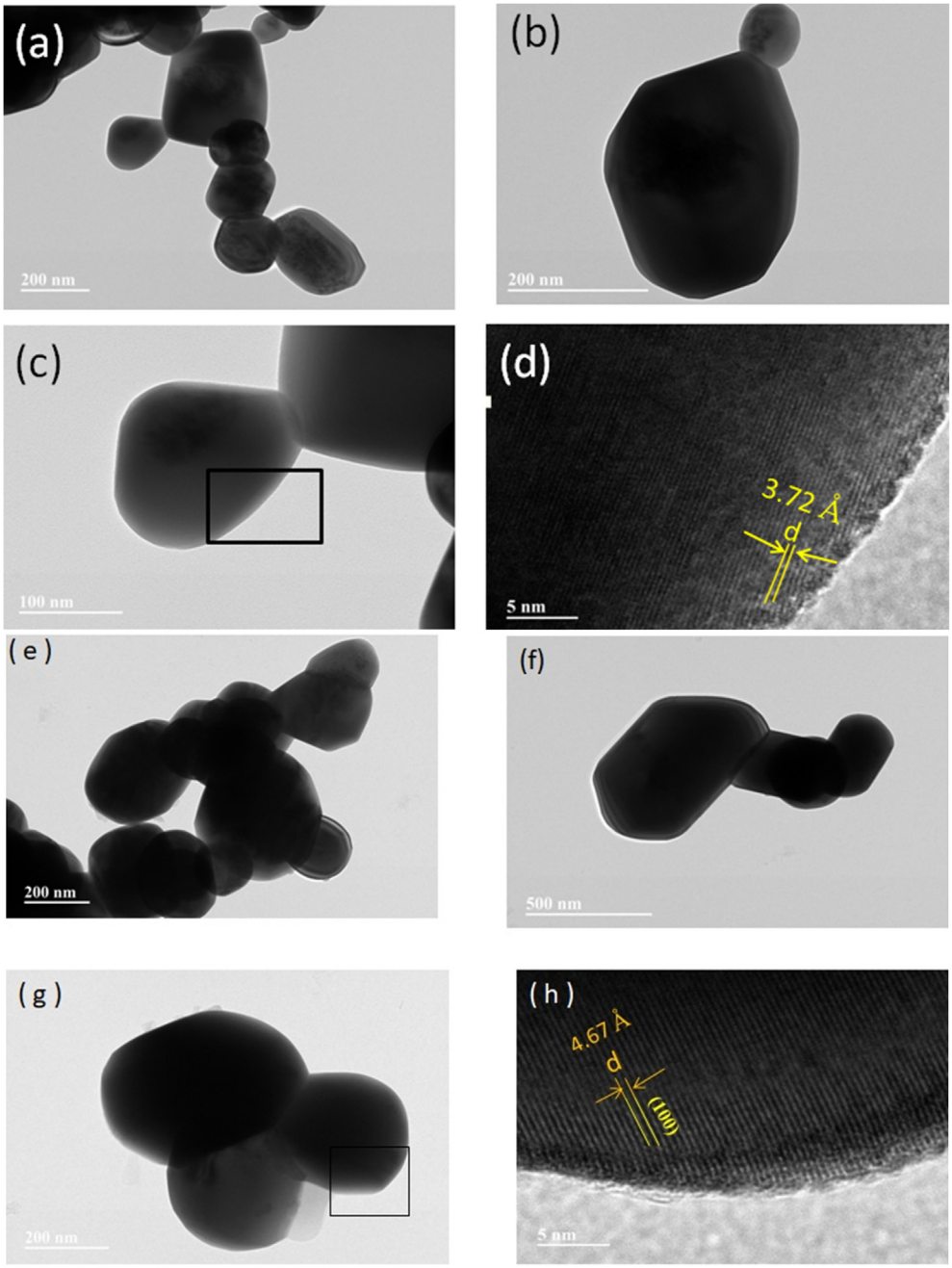

Fig. 8. TEM images of $CoWO_4$ crystals synthesized by the (a,b,c) CP and (e.f,g) (PP) methods, and HR-TEM images for $CoWO_4$ crystals synthesized by the (d) CP and (h) (PP) methods, respectively.

$CoWO_4$ crystals prepared by the PP method exhibit a more anisotropic than isotropic growth than isotropic. Moreover, the HR-TEM image in Fig. 8(h) showed the presence of some $CoWO_4$ crystals with diameters of approximately 600 nm. Finally, the Fig. 8(h) shows the interplanar distance for these crystals was estimated at around 4.67 Å, which correspond to (1 0 0) crystallographic plane of $CoWO_4$ monoclinic phase, (edge of a selected small rod-like $CoWO_4$ crystal).

3.6. Optical and colorimetric properties of $CoWO_4$ crystals

The optical band gap energies (E_{gap}) for our $CoWO_4$ crystals obtained by the two synthesis methods were estimated and calculated by a modified Kubelka–Munk equation (11) [122,123]:

$$[F(R_\infty)h\nu] = C_1(h\nu - E_{gap})^n \quad (11)$$

where $F(R_\infty)$ is the Kubelka-Munk function, R_∞ is the reflectance ($R_\infty = R_{sample}/R_{standard}$; $R_{standard}$ refers to barium sulfate [$BaSO_4$]), $h\nu$ is the photon energy, C_1 is a proportionality constant, E_{gap} is the optical band gap, and n is a constant associated with different types of electronic transitions (n = 0.5 for directly allowed, n = 2 for indirectly allowed, n = 1.5 for directly forbidden, and n = 3 for indirectly forbidden) [124]. Therefore, the E_{gap} values for our $CoWO_4$ sub-microcrystals and microcrystals were calculated with a basis in previous literature proven by means of theoretical calculations at density functional theory (DFT) [73], which indicates the optical diffuse reflectance UV–Vis spectra governed by direct electronic transitions. In this phenomenon, after the electronic absorp-

tion process, electrons located in minimum energy states in the conduction band (CB) can relax to the maximum energy states of the valence band (VB) in a same *k*-points in the Brillouin zone [73,125]. Based on this information, the E_{gap} values of the $CoWO_4$ crystals were calculated using $n = 0.5$ in equation (11). We plotted values of $[F(R_\infty)h\nu]^2$ against $h\nu$, and, using equation (11), $E_{gap(exp)}$ values were estimated by extrapolating the linear portion of UV–Vis curve to the *y*-axis intercept.

Fig. 9(a,b) display the UV–Vis diffuse reflectance spectra of $CoWO_4$ crystals obtained by the CP and PP methods, respectively. Insets show the E_{gap} values and the digital photos of these crystals.

As displayed in Fig. 9(a,b), the profiles of UV–Vis spectra of $CoWO_4$ crystals indicated a typical optical behavior found in

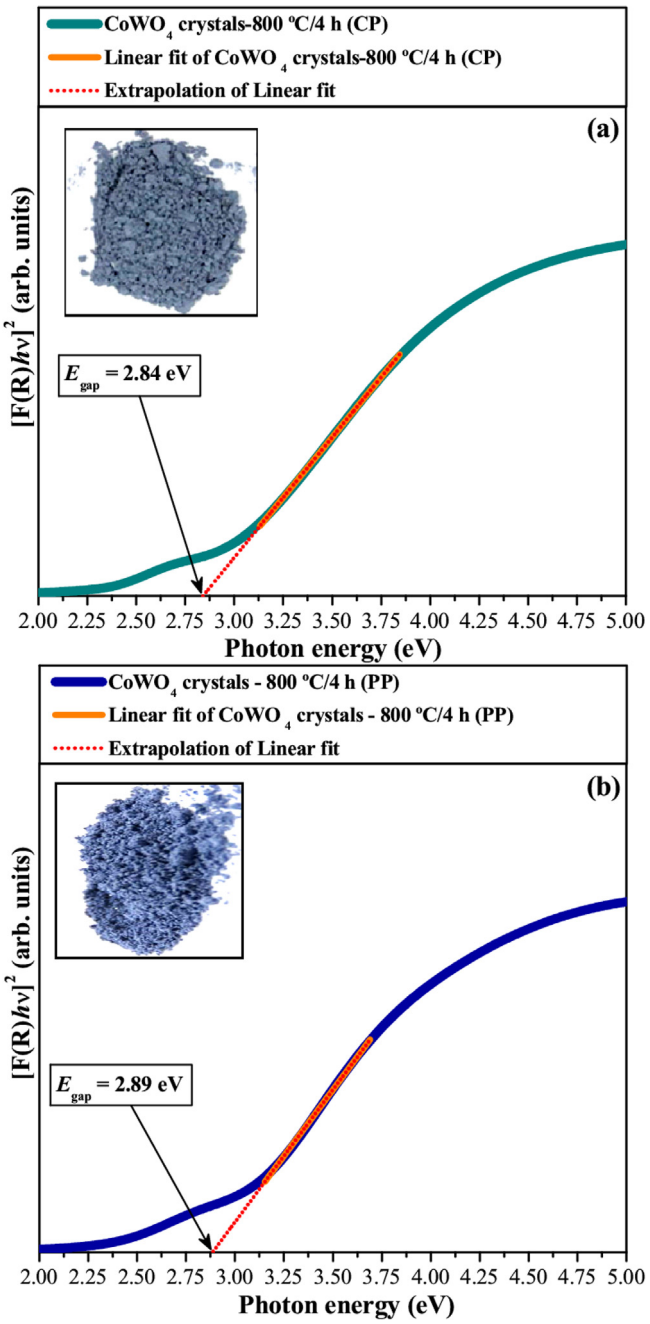

Fig. 9. UV–Vis spectra for $CoWO_4$ crystals synthesized by the (a) CP and (b) PP methods. Insets show the digital photos of $CoWO_4$ crystals obtained by each method, respectively.

structurally-ordered crystalline materials. Such $CoWO_4$ crystals present a direct optical band gap with (E_{gap} = 2.84 and 2.89 eV) values. This small deference at ΔE_{gap} = 0.05 eV values between our $CoWO_4$ crystals is possibly related to the Jahn-Teller effect, intermediary electronic levels, or electronic structure defects, as previously explained in Fig. 3(a,b) and Fig. 4(a–f). Moreover, a small shoulder was observed at ~2.65 eV in both $CoWO_4$ crystals, which is possibly due to the presence of defect states in the band gap. For the transition metal tungstates, the 2*p* orbitals (O atoms) are predominant in the maximum valence band (VB), while the minimum conduction band (CB) is predominantly composed of 3*d* orbitals (Co atoms) and 5*d* orbitals (W atoms) [73]. These two crystalline oxide absorbs visible light with a wavelength smaller than 425 nm, due to their low-values band gap (2.84 < 2.89 < ~2.92 eV). According to the data reported in the literature [38,41,61,73,126–129], the $CoWO_4$ crystals prepared experimentally and theoretically calculated present different optical band gap values ranging from 2.20 eV to 3.20 eV. This feature can be related to the influence of different synthesis methods, shapes, and average crystal sizes for $CoWO_4$ (Table 4).

As can be seen in Table 4, all experimentally obtained results in our study are in good agreement with the literature [38,41,61,126–129]. Some small differences in E_{gap} values can be ascribed to electronic structure defects, resulting in different arrangements of electronic energy levels located between the VB and CB. Moreover, our $CoWO_4$ crystals prepared by the CP method exhibited a smaller E_{gap} value, suggesting a major presence of surface and structural defects at the medium range and local bond distortions which yield localized electronic levels within the forbidden bandgap.

The colorimetry analysis was realized by means of CIELAB color space defined by the International Commission on Illumination (CIE) in 1976 [130]. The color measurements were performed in three readings on an angle of 90° for each sample, obtaining an average of the five readings (L^*, a^*, and b^*) as displays at 2D-circle and 3D-sphere color scales in Fig. 10(a,b) for $CoWO_4$ crystals obtained by the CP and PP, respectively.

CIELAB data is the most popular color space and recognized worldwide, using a white standard as a reference through a colorimeter for measuring object color and is widely used in the literature [21,72,131]. Although, it is possible to perform this kind of approximate measurement to obtain CIELAB data using a smartphone app named Colorimeter at version 5.5.1 (developed by Research Lab Tools, São Paulo, Brazil; purchased from Google Play) [132]. This uniform color space was defined by CIE in 1976 to reduce one of the major problems of the original *Yxy* space: that equal distances on the *x*, *y* chromaticity diagram did not correspond to equal perceived color differences. In this color space, L^* indicates lightness and a^* and b^* are the chromaticity coordinates. The a^* colorimetry coordinate corresponds to ($-a$ = green color) and ($+a$ = red color) at values in the *x*-axis, b^* colorimetry coordinate corresponds to ($-b$ = blue color) and ($+b$ = yellow color) at values in the *y*-axis, and L^* is lightness, which may vary (from 0 = black to 100 = white) in value on the *z*-axis [133,134]. Our two $CoWO_4$ sub-microcrystals and microcrystals prepared by PP method obtained higher L^* and a* values while having smaller b^* values. These results may be attributed to the crystals size and shape. The difference in blue pigmentation in $CoWO_4$ crystals was visibly observed of qualitatively form previously through digital photos (Inset Fig. 9(a,b)). However, qualitative data with more details are proved by means of mathematical localization (a^*,b^*) color coordinates at 2D-circles and (L*) coordinates at 3D-sphere color scales in Fig. 10(a,b) for $CoWO_4$ sub-microcrystals and microcrystals obtained by the CP and PP methods. The changes of pigment were well correlated concerning to all color parameters (L^*, a^*, b^*). These color coordinates values were obtained by the color software FRU® version 3.22, and high-quality digital photos of

Table 4
Comparative results between the morphological features (crystal size and shape) and optical band gap energy (E_{gap}) values of $CoWO_4$ crystals synthesized by the CP and PP methods, followed by heat treatment at 800 °C for 4 h obtained in the present work and those reported in the literature.

Synthesis method	T (°C)	*t* (h)	Crystal shape	Average crystal size (nm)	E_{gap}(eV)	*Ref.*
HC	180	24	Spherical	50	2.61	[38]
CP-C	500	1	Nearly spherical	30–50	2.95	[41]
MF	1250	15	Single crystals	4000	2.80	[61]
DFT	–	–	–	–	3.20	[73]
SASRFC	500	1	Spherical	70	2.58	[126]
CP-C	400	4	Spherical agglomerates	2000	2.20	[127]
CP-C	500	1	Spherical	–	2.86	[128]
PAHC	150	15	Spherical	25	2.40	[129]
CP	800	4	Quasi-spherical and Ellipse-like	150–375	2.84	✠
PP	800	4	Rod-like and Quasi-spherical-like	600–1500	2.89	✠

T = Temperature; *t* = time; HC = hydrothermal conventional; CP-C = Co-Crecipitation with calcination; MF = Melted Flux; DFT = density-functional theory; SASRFC = Salt aqueous solution reaction followed by calcination; PAHC: Precipitation assisted hydrothermal conventional; CP = Co-Crecipitation; PP = Polymeric precursor; *Ref.* = References; and ✠= This Work.

our $CoWO_4$ crystals were used to obtain *RGB* values, presented in Table 5, employing the Color Detector - Instant Color Detect 1.0.1 for Windows for this visual qualitative observation.

As noted in Table 5, we obtained the L^*, a^*, and b^* values, and calculated the energy difference (ΔE), Chroma (C), and the Hue angle (H) utilizing of equations (12–14) below:

$$\Delta E = \sqrt{(\Delta L*)^2 + (\Delta a*)^2 + (\Delta b*)^2} \quad (12)$$

$$C = \sqrt{(a*)^2 + (b*)^2} \quad (13)$$

$$H = tan^{-1}(\frac{b*}{a*}) \quad (14)$$

where ΔE is the energy difference between color media, ΔL is the difference in brightness between two vivid surfaces, and Δa^* and Δb^* are the differences in the color coordinates a^* and b^*, respectively. C is related to the vividness or dullness of a color or how close the color is to either gray or the pure hue. Finally, H is one of the main properties (called color appearance parameters) of color and describes how color is similar to or different from stimuli that are described as red (R), green (G), blue (B), or yellow (Y).

As seen in Table 5, we found that the $CoWO_4$ sub-microcrystals and microcrystals prepared by the PP method exhibit higher L^* and a^* values, while smaller b^* values. The color results may be attributed to the E_{gap} values, particle size, and shape. The difference in B pigmentation of our oxides area desinenged as (● for $CoWO_4$ crystals prepared by CP method) and (■ for $CoWO_4$ crystals prepared by PP method), as shown in (inset Fig. 10(a,b)), Fig. 9(a,b) and in the *RGB* color values in Table 5. The changes in the $CoWO_4$ blue pigment were well correlated concerning all the color parameters L^*, a^*, b^*. Finally, we have noted that though there are a few studies that have reported details of the colorimetric properties of $CoWO_4$ crystals [21,72], these papers only briefly describe their colors: blue, bluish purple to dark ones, respectively. However, in this work, we have investigated in more detail their structure, morphologies, optical band gap, color name, colorimetric coordinates and in the final topic the supercapacitors properties.

3.7. Supercapacitor properties

The electrochemical investigations for supercapacitor (SC) properties of nanocrystalline $CoWO_4$ electrodes were investigated using a three-electrode cell with 1.0 mol L^{-1} of Na_2SO_4 aqueous solution as the electrolyte. Fig. 11(a,b) show the CV curves of two $CoWO_4$ electrodes at a scan rate of 20 mV s^{-1} over different potential window from 0.4, 0.6, 0.8, and 1.0 V vs Ag/AgCl.

According to the recente literature [135], the better electrochemical performance of the active material is obtained by the larger area of CV curve. As shown in Fig. 11(a,b), the area of the $CoWO_4$ electrodes prepared by different synthesis CP and PP methods prepared was determined for a potential range, in which the redox peaks were more clearly observed [53]. Furthermore, CV was used to determine the potential range in which the asymmetric supercapacitor can operate without significantly undergoing oxidation/reduction reactions, i.e., oxygen and/or hydrogen evolution reaction, and also to calculate the specific capacitance.

The CV curves of two $CoWO_4$ electrodes at a scan rate of 20 mV s^{-1} over the different potential windows from 0.4, 0.6, 0.8, and 1.0 V vs Ag/AgCl as displayed in Fig. 11(a,b). Moreover, a pair of symmetric redox peaks related to two oxidation states of $Co^{II}WO_4/Co^{III}WO_4$ electrodes at (oxidative sweep: $Co^{2+} \rightarrow 1e^- + Co^{3+}$) and (reductive sweep: $Co^{2+} \leftarrow 1e^- + Co^{3+}$) were observed on each CV curve, indicating that the capacitance characteristics are mainly governed by the surface faradaic redox mechanism [53]. Since then, it was carried out the potential window from 0.0 to 0.4 V for specific capacitance (C_s) analysis.

The supercapacitor behavior was integrally dependent on scan rates in an inert electrolyte (pH ~ 7) performed in 1 mol L^{-1} Na_2SO_2 solution. In order to evaluate the electrochemical properties, capacitance and CV measurements in $CoWO_4$ electrode film prepared by the CP and PP methods. Fig. 12(a,b) shows CV curves in a potential window from 0 to 0.4 V at different scan rates from 5 to 100 mV s^{-1} and Fig. 12(c) shows the capacitance as a function of the scan rate, which was calculated by the Equation (15) [74]:

$$C_s = \frac{1}{m\upsilon(V_c - V_a)} \int_{V_a}^{V_c} I(V)dV \quad (15)$$

where C_s is the specific capacitance (F g^{-1}), m mass of the active material (g), υ is the scan rate (mV s^{-1}), V_c is the low potential (V) and V_a is the high potential (V), and I (A) is the instant current on CV curves, respectively.

The supercapacitor behavior was integrally dependent on scan rates in an inert electrolyte (pH ~ 7). Fig. 12(a,b) display the electrodes reached a large magnitude current density of 4 mA and −4 mA for $CoWO_4$ electrode film prepared by the CP method and 1.5 mA and −2.5 mA for $CoWO_4$ electrode film prepared by the PP method by using potentials of 0.0 V and 0.4 V, respectively, at high scan rates. Though, even in a high scan rate, the more rectangular symmetrical shape of $CoWO_4$ electrode film prepared by the CP method was maintained, which indicating a good performance for cycles of charging ↔ discharging of this material oxide at elevated voltages [136]. As shown in Fig. 12(c), the C_s for $CoWO_4$ electrode film prepared by the CP method are 160.5, 173.9, 188.4,

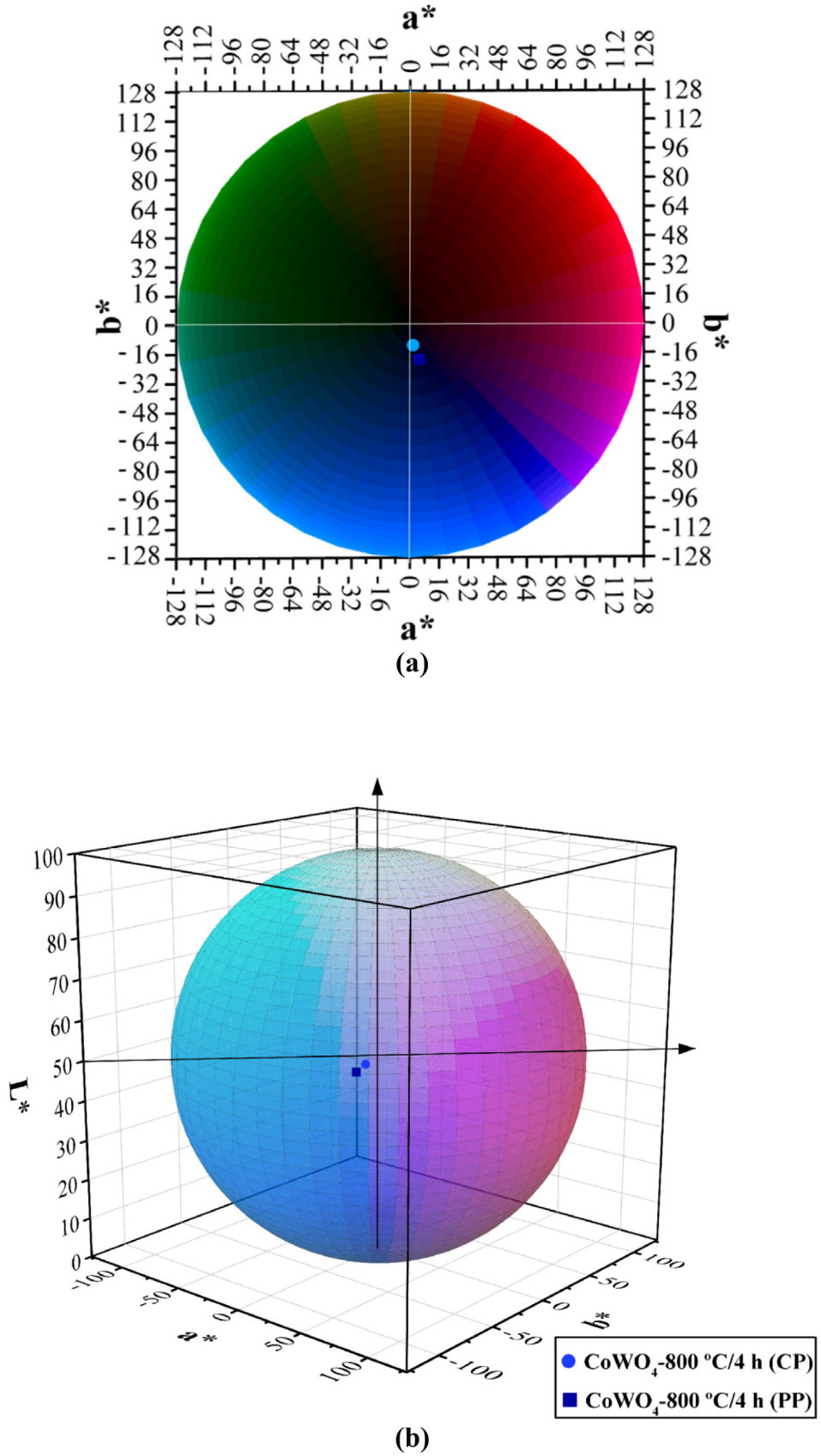

Fig. 10. CIELAB (1976) with L^*, a^*, b^* chromaticity diagram in (a) 2D circle shape and (b) 3D sphere shape for $CoWO_4$ crystals synthesized by the (a) ● CP and ■ PP methods, respectively.

Table 5
Colorimetric coordinates (L^*, a^*, b^*, ΔE^*, C^*, H^*, ΔL^*, Δa^*, Δb^*, ΔE^{**}, ΔC^{**}, and ΔH^{**} values), *RGB* values, HEX codes, and color names for $CoWO_4$ crystals synthesized by the CP and PP methods.

SM	L*	a*	b*	ΔE	C*	H*	RGB Measured	HEX Measured	*Nearest color found	**Nearest color observed	RGB* Observed	HEX Observed
CP	48.734	0.763	−12.520	–	12.543	−86.51	143;131;101	#6D7489	Slate gray solid	Blue lapis lazuli	45;88;139	#2D588B
PP	45.410	3.03	−19.246	–	19.4837	−81.05	99;107;140	#636B8C	UCLA blue solid	Dark slate blue	47;72;131	#2F4883
SM	***ΔL*****	***Δa*****	***Δb*****	***ΔE****	***ΔC*****	***ΔH*****	–	–	–	–	–	–
CP–PP	3.324	−2.267	6.726	7.8375	−6.9407	−5.46	–	–	–	–	–	–

SM = Synthesis methods; CP = Co-Precipitation; PP = Polymeric precursor; CP–PP = Difference color data between the synthesis methods; L = Luminosity, a^* (+a^* indicates the red color and −a^* indicates the green color); b^* (+b^* indicates the yellow color and −b^* indicates the blue color); ΔE = energy difference between samples; C = Chroma; and H = the hue angle, *RGB* = is the abbreviation of an additive color system in which *R* is the red, *G* is the green, and *B* is the blue, HEX = is the abbreviation for the hexadecimal notation of the colors, *Obtained with Color Software FRU® version 3.22 and ** Color detector - instant color detect version 1.01.

192.5, 111.8, 108.9 and 97.2 at the scan rates of 5, 10, 20, 40, 60, 80 and 100 mV/s, respectively; and those for the $CoWO_4$ electrode film prepared by the PP method are 249.1, 90.1, 66.5, 54.9, 49.9, 58.9 and 44.5 Fg^{-1} at the same corresponding scan rates. The decrease in C_s with increasing scan rate is attributed to unable the full accessibility of electrolyte ions to the interior surfaces of the active materials for charge-storage due to the reduced diffusion time at a high scan rate. In addition, the C_s for $CoWO_4$ electrode film prepared by the PP method are much higher than those for $CoWO_4$ electrode film prepared by the CP method, only at 5 mV s^{-1} and smaller at the others scan rate, implying that the $CoWO_4$ structure, morphological, small size, active site and narrow particle size distribution influence to the supercapacitive performances of the $CoWO_4$ electrode. The *Cs* for as-prepared $CoWO_4$ electrode film prepared by the CP method (160.5 Fg^{-1} at 5 mV/s) is also much higher than those for Co-based metal tungstate, such as $CoWO_4$ nanocrystalline (60.6 Fg^{-1} at 5 mV/s) [52] and $CoWO_4$ nanosheets (156 Fg^{-1} at 5 mV/s) [52] and for as-prepared $CoWO_4$ electrode by the other PP method also higher modified $CoWO_4$, such as graphene oxide/$CoWO_4$ nanocomposites (159.9 Fg^{-1} at 5 mV/s) [52], and $0.2CoWO_4$–$0.8NiWO_4$ nanocomposites (196.7 Fg^{-1} at 20 mV/s) [43] and higher pure $CoWO_4$ crystals, such as $CoWO_4$ nanocrystalline (231.1 Fg^{-1} at 50 mV/s) [51]. A comparison with different methods previously reported in the literature for the preparation of $CoWO_4$ electrode films and their respective *Cs* at different scan rates is presented in Table 6.

As can be presented in Table 6 above, we have noted some well significant differences in C_s values for pure $CoWO_4$ crystals and modified $CoWO_4$ crystals when compared with other previous papers reported in the literature [26,39,40,43,51,52, 53,54,135,137–147] of the crystalline and amorphous state. These differences at minor C_s values that have already been previously reported in the literature [43,51,52,138,143,145,146,147] about our $CoWO_4$ crystals can be possibly ascribed to the relatively slower redox rates on the cobalt actives sites, cobalt deficiencies or oxygen vacancies. Moreover, based on our previous experimental and theoretical analysis is noted the presence of the effect of order–disorder at the monoclinic lattice through Rietveld refinement data at the long-range, non-homogeneous distribution of electronic charges on surfaces mainly for $CoWO_4$ nanocrystals prepared by the CP method, Raman-active vibrational modes are not well-sharp or defined at Raman spectra at short-range, distortions in the between (O–W–O) and (O–Co–O) bonds found in FT-IR spectra. Specific intermediary levels between the VB and CB with the indirect electronic transition for this *p*-type semiconductor, in this case, $CoWO_4$ microcrystals prepared by the PP method, as be employed more effectively as a supercapacitor.

Moreover, the $CoWO_4$ crystals as electrodes is a *p*-type semiconductor with an anisotropic lattice monoclinic and exhibits structural defects to long, short, and medium-dystranic as previously shown by means of Rietveld refinement data, micro-Raman spectra, IR spectra and UV–Vis data spectroscopy. In the neutral state its crystal lattice is formed by the interconnection of octahedral $[WO_6]^x_o$–$[CoO_6]^x_o$ ordered or organized clusters with and octahedral $[WO_6]^x_d \leftrightarrow [CoO_6]^x_d$ disordered or very distorted clusters. If an oxidation reaction occurs in $CoWO_4$ crystals surface as electrode it loses electrons (*e*-) and the band gap increases and in reduction processes when it gains *e*- the bandgap decreases. The reduction and oxidation processes at the surface of $CoWO_4$ crystals as electrodes crystals by means clusters notation follow the equations (16–18) is oxidation processes, and (19–21) is reduction processes below:

$$[WO_6]^x_o - [CoO_6]^x_o \rightarrow [WO_6]^x_o - [CoO_6]^{\cdot}_o + 1e^- \quad (16)$$

$$[WO_6]^x_d - [CoO_6]^x_d \rightarrow [WO_6]^x_d - [CoO_6]^{\cdot}_d + 1e^- \quad (17)$$

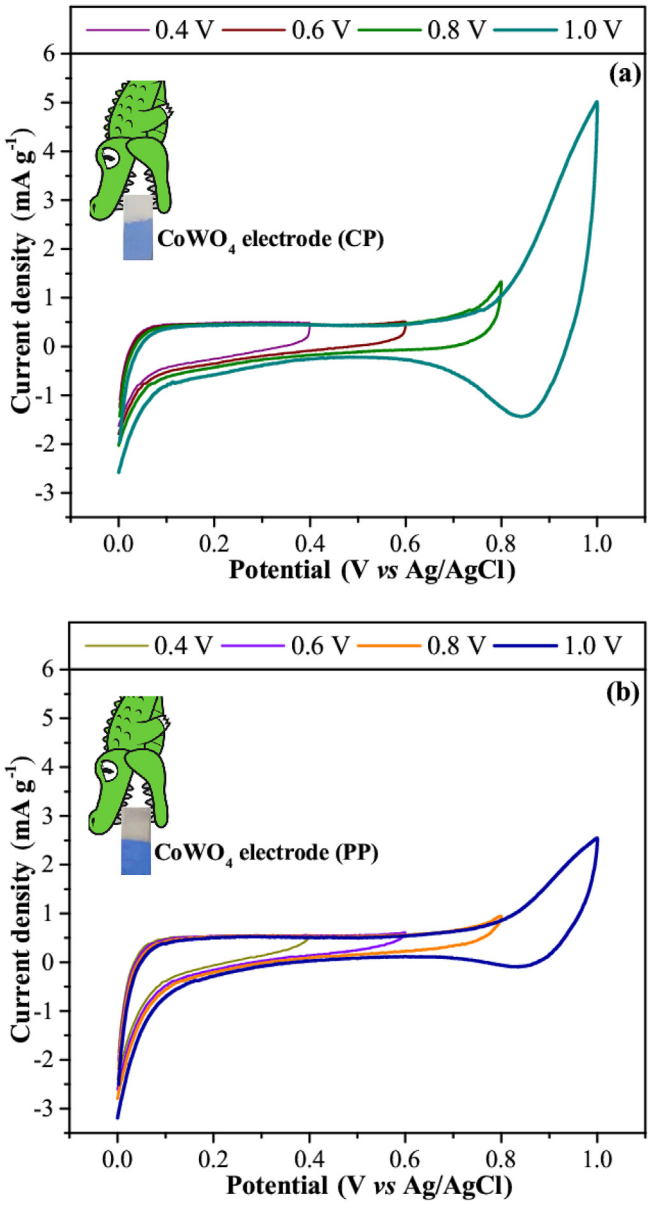

Fig. 11. Cyclic voltammetry (CV) curves (a) $CoWO_4$ as electrode crystals prepared by CP method and (b) $CoWO_4$ as electrode crystals prepared by CP method PP electrodes at different potential range, respectively. The inset shows the claw used to hold the $CoWO_4$ electrode film.

$$[WO_6]_d^x - [CoO_5.V_O^x]_d \rightarrow [WO_6]_o^x - [CoO_5.V_O^{\cdot}]_d + 1e^- \quad (18)$$

$$[WO_6]_o^x - [CoO_6]_o^x + 1e^- \rightarrow [WO_6]_o^x - [CoO_6]_o^{e-} \quad (19)$$

$$[WO_6]_d^x - [CoO_6]_d^x + 1e^- \rightarrow [WO_6]_d^x - [CoO_6]_d^{e-} \quad (20)$$

$$[WO_6]_d^x - [CoO_5.V_O^{\cdot}]_d + 1e^- \rightarrow [WO_6]_o^x - [CoO_5.V_O^x]_d \quad (21)$$

where the octahedral $[WO_6]_o^x$ ordered clusters and distorted octahedral $[WO_6]_d^x$ disordered clusters that form the lattice remain with their oxidation state unchanged during the oxidation and reduction

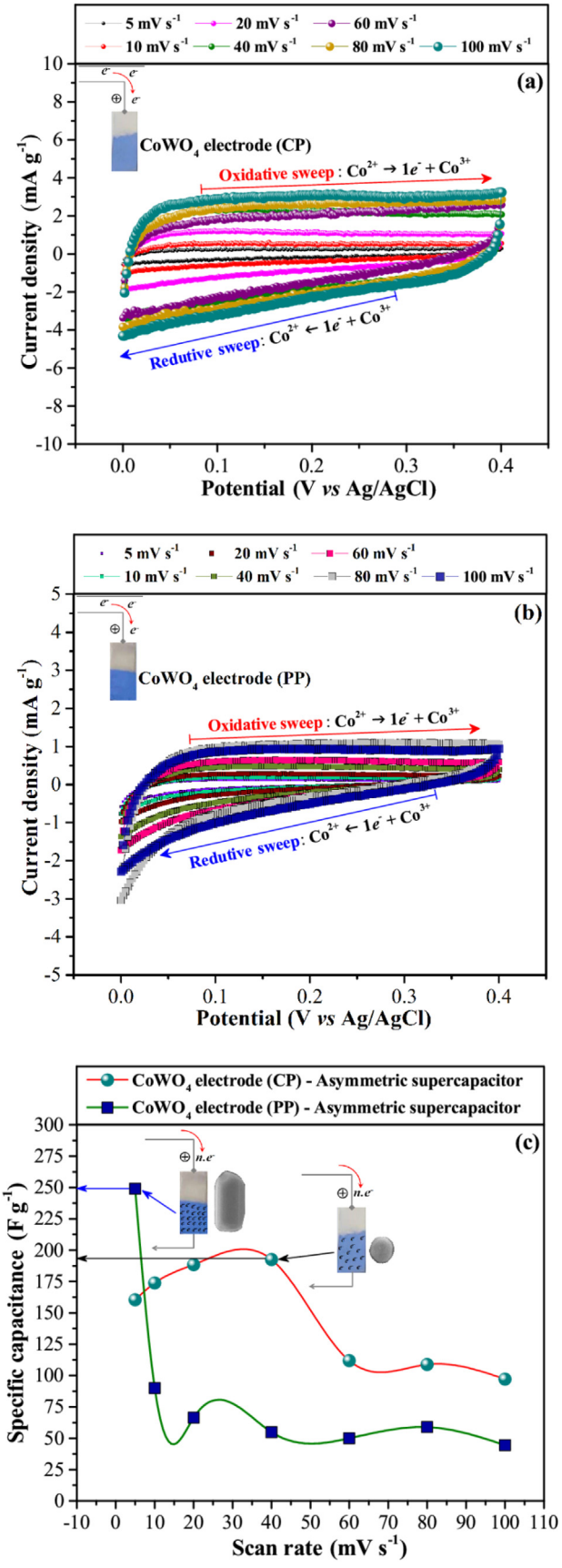

Fig. 12. (a,b): Cyclic voltammograms for (a) $CoWO_4$ as electrode crystals prepared by CP method and (b) $CoWO_4$ as electrode crystals prepared by CP method PPM electrodes at different scan rates from 5 to 100 mV s^{-1} in 1 mol L^{-1} Na_2SO_4 solution and (c) Specifc capacitance as a function of the scan rate, respectively. Inset shows the $CoWO_4$ electrode film during the oxidation ↔ reduction process and the electron storage process such as the $CoWO_4$ cathode electrode for supercapacitors.

Table 6
Electrochemical data of different $CoWO_4$ crystals reported in the literature with those obtained in the present work, which can be employed as an alternative material for supercapacitors.

Material	Synthesis method	Temp. (°C)	*t* (h)	Electrolyte type	Scan Rate (mV s^{-1})	C_s (Fg^{-1})	*Ref.*
$CoWO_4$/rGO/$CoWO_4$ composites	Jet nebulized spray pyrolysis method	450	2	Na_2SO_4	5	500	[26]
3D heterostructure $CoWO_4$/Co_3O_4 nanowires	Efficient microwave hydrothermal method/calcination	400	2	KOH	5	1728	[39]
$CoWO_4$ nanoparticles	Efficient microwave hydrothermal method	110	0.5	KOH	5	496	[40]
3D heterostructure $CoWO_4$/Co_3O_4 nanocone	Efficient microwave hydrothermal method/calcination	400	2	KOH	5	1728	[40]
$CoWO_4$ nanoparticles	Simple chemical coprecipitation method	70	12	KOH	20	74.8	[43]
0.2$CoWO_4$–0.8$NiWO_4$ nanocomposites	Simple chemical coprecipitation method	70	12	KOH	20	196.7	[43]
$CoWO_4$ nanocrystalline	Hydrothermal method	180	8	KOH	50	231.1	[51]
$CoWO_4$ nano-shuttles/Ni foam	Hydrothermal method	180	8	KOH	50	764.4	[51]
$CoWO_4$ nanocrystalline	One-pot hydrothermal method	180	12	KOH	5	60.6	[52]
graphene oxide/$CoWO_4$ nanocomposites	One-pot Hydrothermal method	180	12	KOH	5	159.9	[52]
$CoWO_4$-amorphous	Wet-chemical method	60	12	KOH	5	403	[53]
$CoWO_4$-crystalline	Hydrothermal method	160	12	KOH	5	264	[53]
$CoWO_4$ nanospheres	Hydrothermal method	160	18	KOH	5	1446.5	[54]
Carbon nanotubes-$CoWO_4$ nanocomposite	Hydrothermal method	160	18	KOH	5	1486.5	[54]
3D hollow Flower-like $CoWO_4$/Ni-foam	Hydrothermal method/ Calcination	350	2	KOH	5	1395	[55]
$CoWO_4$ nanoflakes	Hybrid transition metal oxides method	300	5	KOH	5	885.6	[135]
$CoWO_4$/$CoMn_2O_4$ nanoflakes composite	Hybrid transition metal oxides method	300	5	KOH	5	2259.6	[135]
$CoWO_4$ nanoparticles	Chemical precipitation reaction method	75	2	H_2SO_4	2	378	[137]
$CoWO_4$ nanopowders	Simple microwave irradiation method	500	2	KOH	100	45	[138]
$CoWO_4$ nanosheets	Simple hydrothermal method	150	6	KOH	5	1127.6	[139]
Dandelion-Like Co_3O_4/ $CoWO_4$ heterojunctions	Hydrothermal method	180	5	KOH	5	331.6	[140]
$CoWO_4$ nanosheets	Two-step hydrothermal method	130	10	KOH	50	289.6	[141]
Hybrid Rod-Like Hollow $CoWO_4$/Co-1xS	Two-step hydrothermal method	130	10	KOH	10	1894.5	[141]
Hierarchical CuAl-layered double hydroxide/ $CoWO_4$ nanocomposites	Solvothermal Method	110	12	KOH	5	675	[142]
$CoWO_4$ nanosheets	Hydrothermal method	150	10	KOH	5	156	[143]
$CoWO_4$/$NiCo_2O_4$ nanostructures	Hydrothermal method/Calcination	350	3	KOH	10	1923	[144]
$CoWO_4$ nanoparticles	Wet chemical method	80	2	KOH	10	128	[145]
$CoWO_4$/Ni nanocomposite	Wet chemical method	80	2	KOH	10	271	[145]
$CoWO_4$ nanoparticles	Hydrothermal method	180	12	KOH	50	56.6	[146]
$CoWO_4$ nanoparticles /Co − B20wt% nanoparticles	Hydrothermal method/wet-chemical precipitation method/Reuction with BH_4	180	12	KOH	50	177.4	[146]
S-doped $CoWO_4$ nanospheres	Simple and scalable one step hydrothermal method	140	10	KOH	2	177.25	[147]
$CoWO_4$ nanocrystals	Co-Precipitation method	800	4	Na_2SO_4	40	192.5	✠
$CoWO_4$ nanocrystals	Polymeric precursor method	800	4	Na_2SO_4	5	249.1	✠

Temp. = Temperature; *t* = time; C_s = Specific Capacitance; *Ref.* = References; and ✠= This Work.

process. Therefore, the shape of $CoWO_4$ crystals as electrodes and degree of anisotropy plays a fundamental role in receiving or donating electrons into electrochemical properties, as each surface has different bandgap energy, thus our $CoWO_4$ sub-microcrystals and microcrystals prepared by the CP and PP methods have different efficiency as cathode material for asymmetric supercapacitors in good agreement with the recent literature [148,149,150] and compared with other oxides-related and hybrid materials [151–154].

4. Conclusions

In summary, we successfully obtained pure and monophasic $CoWO_4$ crystals prepared by the CP and PP methods, followed by treated at 800 °C for 4 h. These crystals were structurally and morphologically characterized by XRD patterns, Rietveld refinement analysis, Micro-Raman/FT-IR spectroscopies, FE-SEM, TEM, and HR-TEM images. XRD patterns and Rietveld refinement data confirmed the formation of pristine $CoWO_4$ crystals with a wolframite-type monoclinic structure with ($P2/c$) space group and symmetry point group (C_{2h}^4). The employed of different synthesis methods promoted a change in bond lengths and/or distortions in bond angles of octahedral [CoO_6]/[WO_6] clusters. Our electron density maps showed a major inhomogeneous distribution of charges between distorted octahedral [CoO_6] clusters in the (1 2 1) plane for $CoWO_4$ crystals prepared by the PP method. FE-SEM, TEM and HR-TEM images showed that $CoWO_4$ crystals prepared by the PP method exhibit a morphology driven by a growth process that is more anisotropic than $CoWO_4$ crystals prepared by the CP method with a quasi-spherical shape. The effect of crystal size on the structural distortions was observed clearly in the bond angles of the clusters. The direct optical E_{gap} values were estimated by the modified Kubelka-Munk function as 2.84 and 2.89 eV, corroborated by values found in the literature, which indicates the capacity to absorb visible light. The changes in the E_{gap} values are likely due to the increase in octahedral distortion due to intermediary electronic levels between the VB and CB. Moreover, a good correlation and with only small differences in the L^*, a^*, and b^* CIE-LAB color coordinates between the $CoWO_4$ crystals obtained by the CP and PP methods, with slate gray solid and UCLA blue solid colors, respectively. However, the colors observed by the color detector software are more similar to blue lapis lazuli and dark slate blue. Based on our results, we believe that these oxides can be applied as inorganic colored pigments. Finally, we demonstrated an electrochemical behavior to $CoWO_4$ electrodes, which exhibited a specific capacitance of 192.5F g^{-1} at 40 mV $s^{-1}$for $CoWO_4$ crystals prepared by the CP method, and 249.1F g^{-1} at 5 mV $s^{-1}$for $CoWO_4$ crystals prepared by the PP method. Therefore, our $CoWO_4$ cathode electrodes showed significant specific capacitance values, which become promising materials for use in supercapacitors.

Declaration of Competing Interest

The authors declare that they have no known competing financial interests or personal relationships that could have appeared to influence the work reported in this paper.

Acknowledgments

The Brazilian authors acknowledge the financial support from the Brazilian research financing institutions: CNPq (312318/2017-0 and 408036/2018-4), CCN2-PPGCM-UFPI-LIMAV, GERATEC-UESPI-CETEM, FAPESP-CDMF (13/07296-2) and CAPES. A.F.G acknowledges the Universitat Jaume I for the postdoctoral contract (POSDOC/2019/30).

References

[1] I.V. Pekov. Minerals first discovered Lon the territory of the former Soviet Union, 1998, Vol. 1.
[2] M. Okrusch, S. Matthes, Eine Einführung in die spezielle Mineralogie, Petrologie und Lagerstättenkunde, Springer Spektrum, 2014.
[3] F. Caporuscio, Minerals first discovered on the territory of the former Soviet Union, Am. Mineral. 91 (2006) 487–488.
[4] C. Pimentel, J.H.E. Cartwright, C.I. Sainz-Díaz, A tungstate chemical garden, ChemSystemsChem 2 (2020) e2000023–e2000026.
[5] B.V. Chesnokov, L.F. Bazhenova, E.P. Shcherbakova, T.A. Michal, T.N. Deriabina. *New minerals from the burned dumps of the Chelyabinsk coal basin, in Mineralogy, technogenesis, and mineral-resource complexes of the Urals*, 1988, Akad. Nauk SSSR-Uralskoe Otdel.
[6] B. Cesnokov, M. Kotrly, T. Nisanbajevm, *Brennende Abraumhalden und Aufschlüsse im Tscheljabinsker Kohlenbecken - eine reiche Mineralienküche*, 1998, *Mineralien-Welt*, 9(3), p. 54–63.
[7] J. Wu, R. Xie, X. Hu, Z. Nie, Y. Shi, Y. Yu, N. Yang, High-performance overall water splitting based on amorphous iron doped cobalt tungstate via facile co-precipitation, J. Mater. Chem. A 9 (2021) 9753–9760.
[8] M.A.P. Almeida, L.S. Cavalcante, L.M. Siu, J.A. Varela, E. Longo, Structural refinement and photoluminescence properties of $MnWO_4$ nanorods obtained by microwave-hydrothermal synthesis, J. Inorg. Organomet. Polym. Mater. 22 (2011) 264–271.
[9] M.A.P. Almeida, L.S. Cavalcante, C. Morilla-Santos, P.N. Lisboa Filho, A. Beltrán, J. Andrés, L. Gracia, E. Longo, Electronic structure and magnetic properties of $FeWO_4$ nanocrystals synthesized by the microwave-hydrothermal method, Mater. Charact. 73 (2012) 124–129.
[10] E.-C. Xiao, M. Liu, Q. Ren, Z. Cao, M. Guo, G. Dou, Z.-M. Qi, F. Shi, Phonon characteristics and dielectric properties of a phase pure $CoWO_4$ ceramic, Ceram. Int. 46 (2020) 15705–15708.
[11] M. Yang, C. Zheng, Q. Wang, J. Yin, L. Yang, O. Wang, X. Liu, G. Deng, Improvement of specific capacitance and rate performance of $NiWO_4$ synthesized through modified chemical precipitation, J. Mater. Sci.: Mater Electron. 32 (2012) 12232–12240.
[12] A.F. Gouveia, M. Assis, L.S. Cavalcante, E. Longo, J. Andrés, Reading at exposed surfaces: theoretical insights into photocatalytic activity of $ZnWO_4$, Front. Res. Today 1 (2018) 1005.
[13] E.L. Souza, J.C. Sczancoski, I.C. Nogueira, M.A. Almeida, M.O. Orlandi, M.S. Li, et al., Structural evolution, growth mechanism and photoluminescence properties of $CuWO_4$ nanocrystals, Ultrason. Sonochem. 38 (2017) 256–270.
[14] S.A. Redfern, P.F. Schofield, Order parameter saturation (plateau effect) as a function of composition in the sanmartinite ($ZnWO_4$)-Cuproscheelite ($CuWO_4$) solid solution, Phase Trans. 59 (1996) 25–38.
[15] P.F. Schofield, J.M. Charnock, G. Cressey, C.M. Henderson, An EXAFS study of cation site distortions through the P2/c–P 1 phase transition in the synthetic cuproscheelite-sanmartinite solid solution, Mineral. Mag. 58 (1994) 185–199.
[16] M. Imada, A. Fujimori, Y. Tokura, Metal-insulator transitions, Rev. Mod. Phys. 70 (1998) 1039–1263.
[17] P. Patureau, M. Josse, R. Dessapt, J.-Y. Mevellec, F. Porcher, M. Maglione et al. (2015). Incorporation of Jahn-Teller Cu^{2+} ions into magnetoelectric multiferroic $MnWO_4$: structural, magnetic, and dielectric permittivity properties of $Mn_{1-x}Cu_xWO_4$ ($x \leq 0.25$). *Inorg. Chem.* 2015, *54*, 10623–10631.
[18] V. Perrichon, P. Turlier, Y. Trambouze, Étude cinétique de la synthèse du tungstate de cobalt $CoWO_4$ par réaction a l'état solide, J. Chim. Phys. 65 (1968) 421–427.
[19] R.C. Pullar, S. Farrah, N.M. Alford, $MgWO_4$, $ZnWO_4$, $NiWO_4$ and $CoWO_4$ microwave dielectric ceramics, J. Eur. Ceram. Soc. 27 (2007) 1059–1063.
[20] D. Migas, M. Kierat, G. Moskal, The oxide scales formed on different co-ni based superalloys during isothermal oxidation at 800 and 900 °C. Institute of Metallurgy and Materials Science of Polish Academy of Sciences, Arch. Metall. Mater. 66 (2021) (2021) 5–14.
[21] P. Bělina, V. Machalíková, N. Gorodylova, P. Šulcová, A comparative study of the influence of the method of synthesis of intermediate products in the preparation of $CoNd_2W_2O_{10}$ and $MnNd_2W_2O_{10}$ and their color properties in ceramic glazes. *Chem. Pap.* **2017**, *71*, 1597–1603.
[22] Ríos, T.D.; Martinez, V. C.; Vigil, M.D.; Ortiz, A.L. Synthesis, Characterization and stability performance of $CoWO_4$ as an oxygen carrier under redox cycles towards syngas production. *Int. J. Chem. Reactor Eng.*, **2007**, *5*, 1–12.
[23] B.M. Wanklyn, Flux growth of some complex oxide materials, J. Mater. Sci. 7 (1972) 813–821.
[24] J.A. Bustnes, D. Sichen, S. Seetharaman, Kinetic studies of reduction of CoO and $CoWO_4$ by hydrogen, Metall. Mater. Trans. B 26 (1995) 547–552.
[25] S. Sierra-Perez, N.R. Rojas-Reyes, J. Martinez-Zambrano, H.A. Rojas-Sarmiento, Thermodynamic and kinetic study of the recovery of tungsten and cobalt from tool waste, Rev. Fac. Ing. Univ. Antioq. 89 (2018) 44–51.
[26] P. Dhilip, M. Niththiyanandam, N. Sethupathi, P. Mahalingam, Alternate layers of cobalt doped tungsten oxide and reduced graphene oxide composite as electrode material for supercapacitor, Asian J. Chem 32 (2020) 822–826.
[27] X. Wu, J. Shen, F. Jiang, H. Wu, L. Li, Study on the oxidation of WC-Co cemented carbide under different conditions, Int. J. Refract. Met. Hard Mater. 94 (2021) 105381.
[28] H.V.S.B. Azevêdo, R.A. Raimundo, L.S. Ferreira, M.M. Silva, M.A. Morales, D.A. Macedo, U.U. Gomes, D.G.L. Cavalcante, Green synthesis of $CoWO_4$ powders using agar-agar from red seaweed (Rhodophyta): structure, magnetic properties and battery-like behavior, Mater. Chem. Phys. 242 (2020) 122544.
[29] C.-S. Lim, Solid-state metathetic synthesis of MWO_4 (M=Zn, Co) particles assisted by microwave irradiation, J. Korean Cryst. Growth Cryst. 20 (2010) 295–300.
[30] Q. Diao, F. Yang, C. Yin, J. Li, S. Yang, X. Liang, et al., Ammonia sensors based on stabilized zirconia and $CoWO_4$ sensing electrode, Solid State Ionics. 225 (2012) 328–331.
[31] M. Shekofteh-Gohari, A. Habibi-Yangjeh, Combination of $CoWO_4$ and Ag_3VO_4 with Fe_3O_4/ZnO nanocomposites: magnetic photocatalysts with enhanced activity through *p-n-n* heterojunctions under visible light, Solid State Sci. 74 (2017) 24–36.
[32] M. Mousavi, A. Habibi-Yangjeh, Decoration of Fe_3O_4 and $CoWO_4$ nanoparticles over graphitic carbon nitride: novel visible-light-responsive photocatalysts with exceptional photocatalytic performances, Mater. Res. Bull. 105 (2018) 159–171.
[33] Z. Song, J. Ma, H. Sun, Y. Sun, J. Fang, Z. Liu, et al., Low-temperature molten salt synthesis and characterization of $CoWO_4$ nano-particles, Mater. Sci. Eng. B 163 (2009) 62–65.
[34] S.M. AlShehri, J. Ahmed, T. Ahamad, P. Arunachalam, T. Ahmad, A. Khan, Bifunctional electro-catalytic performances of $CoWO_4$ nanocubes for water redox reactions, RSC Adv. 7 (2017) 45615–45623.
[35] S. Rajagopal, V.L. Bekenev, D. Nataraj, D. Mangalaraj, O.Y. Khyzhun, Electronic structure of $FeWO_4$ and $CoWO_4$ tungstates: first-principles FP-LAPW calculations and X-ray spectroscopy studies, J. Alloys Compd. 496 (2010) 61–68.
[36] L. Zhen, W.-S. Wang, C.-Y. Xu, W.-Z. Shao, L.-C. Qin, A facile hydrothermal route to the large-scale synthesis of $CoWO_4$ nanorods, Mater. Lett. 62 (2008) 1740–1742.
[37] L. Pan, L. Li, Y. Chen, Synthesis and electrocatalytic properties of microsized Ag_2WO_4 and nanoscaled MWO_4 (M=Co, Mn), J. Sol-Gel Sci. Technol. 66 (2013) 330–336.
[38] S. Han, K. Xiao, L. Liu, H. Huang, $Zn_{1-x}Co_xWO_4$ ($0 \leq x \leq 1$) full range solid solution: structure, optical properties, and magnetism, Mater. Res. Bull. 74 (2016) 436–440.
[39] M. Zhang, H. Fan, N. Zhao, H. Peng, X. Ren, W. Wang, et al., 3D hierarchical $CoWO_4/Co_3O_4$ nanowire arrays for asymmetric supercapacitors with high energy density, Chem. Eng. J. 347 (2018) 291–300.
[40] M. Zhang, H. Fan, X. Ren, N. Zhao, H. Peng, C. Wang, et al., Study of pseudocapacitive contribution to superior energy storage of 3D heterostructure $CoWO_4/Co_3O_4$ nanocone arrays, J. Power Sources 2019 (418) (2019) 202–210.
[41] S.J. Naik, A.V. Salker, Solid state studies on cobalt and copper tungstates nano materials, Solid State Sci. 12 (2010) 2065–2072.
[42] de los Ríos Castillo, T.; Gutiérrez, J.S.; Ortiz, A. L.; Collins-Martínez, V. Global kinetic evaluation during the reduction of $CoWO_4$ with methane for the production of hydrogen. *Int. J. Hydrogen Energy*. **2013**, *38*, 12519–12526.
[43] Y. Wang, C. Shen, L. Niu, Z. Sun, F. Ruan, M. Xu, et al., High rate capability of mesoporous $NiWO_4$–$CoWO_4$ nanocomposite as a positive material for hybrid supercapacitor, Mater. Chem. Phys. 182 (2016) 394–401.
[44] X. Xu, J. Gao, G. Huang, H. Qiu, Z. Wang, J. Wu, et al., Fabrication of $CoWO_4$@$NiWO_4$ nanocomposites with good supercapacitve performances, Electrochim. Acta 174 (2015) 837–845.
[45] R.N. Panda, S.B. Dalavi, J. Theerthagiri, Synthesis of high surface area W_2N and Co–W–N nitrides by chemical routes, Adsorpt. Sci. Technol. 30 (2012) 345–354.
[46] S. Shanmugapriya, S. Surendran, V.D. Nithya, P. Saravanan, R.K. Selvan, Temperature dependent electrical and magnetic properties of CoWO4 nanoparticles synthesized by sonochemical method, Mater. Sci. Eng. B. 214 (2016) 57–67.
[47] H.R. Naderi, A. Sobhani-Nasab, M. Rahimi-Nasrabadi, M.R. Ganjali, Decoration of nitrogen-doped reduced graphene oxide with cobalt tungstate nanoparticles for use in high-performance supercapacitors, Appl. Surf. Sci. 423 (2017) 1025–1034.
[48] T. You, G. Cao, X. Song, C. Fan, W. Zhao, Z. Yin, et al., Alcohol–thermal synthesis of flowerlike hollow cobalt tungstate nanostructures, Mater. Lett. 62 (2008) 1169–1172.
[49] S. Thongtem, S. Wannapop, T. Thongtem, Characterization of $CoWO_4$ nano-particles produced using the spray pyrolysis, Ceram. Int. 35 (2009) 2087–2091.
[50] I. Kärkkänen, M. Kodu, T. Avarmaa, J. Kozlova, L. Matisen, H. Mändar, et al., Sensitivity of $CoWO_4$ thin films to CO, Procedia Eng. 5 (2010) 160–163.
[51] G. He, J. Li, W. Li, B. Li, N. Noor, K. Xu, One pot synthesis of nickel foam supported self-assembly of $NiWO_4$ and $CoWO_4$ nanostructures that act as

high performance electrochemical capacitor electrodes, J. Mater. Chem. A 3 (2015) 14272–14278.
[52] X. Xu, J. Shen, N. Li, M. Ye, Facile synthesis of reduced graphene oxide/$CoWO_4$ nanocomposites with enhanced electrochemical performances for supercapacitors, Electrochim. Acta 150 (2014) 23–34.
[53] X. Xing, Y. Gui, G. Zhang, C. Song, $CoWO_4$ nanoparticles prepared by two methods displaying different structures and supercapacitive performances, Electrochim. Acta 157 (2015) 15–22.
[54] V. Lokhande, S.J. Lee, A. Lokhande, J.H. Kim, T. Ji, 1.5 V Symmetric supercapacitor device based on hydrothermally synthesized Carbon nanotubes and Cobalt Tungstate nanocomposite electrodes, Mater. Chem. Phys. 211 (2018) 214–224.
[55] D. Chu, D. Guo, B. Xiao, L. Tan, H. Ma, H. Pang, 3D hollow flower-like $CoWO_4$ derived from ZIF-67 grown on Ni-foam for high-performance asymmetrical supercapacitors, Chem. Asian J. 15 (2020) 1750–1755.
[56] T.N. Rezukhina, T.A. Kashina, Determination of the thermodynamic properties of Co_3W, Co_7W_6, $CoWO_4$, and Co-based solid solutions (Co+W) from a study of solid-electrolyte galvanic cells in the temperature range 1200 to 1360 K, J. Chem. Thermodyn. 8 (1976) 513–517.
[57] K. Tao, H. Dan, Y. Hai, L. Liu, Y. Gong, Ultrafine Co_2P anchored on porous $CoWO_4$ nanofiber matrix for hydrogen evolution: anion-induced compositional/morphological transformation and interfacial electron transfer, Electrochim. Acta 328 (2019) 135123.
[58] Y.-S. Song, J.-H. Chung, S.H. Chun, K.H. Kim, J. Schefer, Competing magnetic anisotropy fields and double polarization flops in multiferroic $Mn_{1-x}Co_xWO_4$, J. Phys. Soc. Jpn. 82 (2013) 124716.
[59] J.J. Joy, Jaya, N.V. (2012). Structural, magnetic and optical behavior of pristine and Yb doped $CoWO_4$ nanostructure. *J. Mater. Sci.: Mater. Electron*. **2013**, *24*, 1788–1795.
[60] M. Jeyakanthan, U. Subramanian, R.B. Tangsali, A. Ramesh, AC conductivity, electrochemical and magnetic studies of $CoWO_4/PbWO_4$ nanocomposites, Physica B: Condensed Matter. 586 (2020) 412151.
[61] R. Bharati, R.A. Singh, B.M. Wanklyn, On electrical transport in $CoWO_4$ single crystals, J. Mater. Sci. 16 (1981) 775–779.
[62] B. Zhang, L. Li, Microstructure and microwave dielectric properties of CuO-modified $CoWO_4$ ceramics, J. Mater. Sci.: Mater. Electron 28 (4) (2017) 3523–3529.
[63] T. Thilagavathi, D. Venugopal, R. Marnadu, J. Chandrasekaran, D. Thangaraju, B. Palanivel, $WO_3/CoWO_4$ nanocomposite synthesis using a facile co-precipitation method for enhanced photocatalytic applications, J. Phys. Chem. Solids 154 (2021) 110066.
[64] K. Jothivenkatachalam, S. Prabhu, A. Nithya, S.C. Mohan, K. Jeganathan, Solar, visible and UV light photocatalytic activity of $CoWO_4$ for the decolourization of methyl orange, Desalin. Water Treat. 54 (2015) 3134–3145.
[65] M. Vosoughifar, Simple route for preparation cobalt tungstate nanoparticles with different amino acids and its photocatalyst application, J Mater Sci: Mater Electron 28 (2017) 8011–8016.
[66] S.-H. Liao, S.-Y. Lu, S.-Jv. Bao, Y.-N. Yu, L. Yu. Electrospinning Synthesis of Porous $CoWO_4$ Nanofibers as an ultrasensitive, nonenzymatic, hydrogen-peroxide-sensing interface with enhanced electrocatalysis. *ChemElectroChem*. 2015, 2, 2061–2070.
[67] Z. Geng, D. Duan, S. Hou, S. Li, Tribological behavior of WC-12Co air plasma-sprayed coating at elevated temperatures, Tribol. Trans. 59 (2016) 55–61.
[68] P. Xing, R. Zhao, X. Li, X. Gao, Preparation of $CoWO_4/g\text{-}C_3N_4$ and its ultra-deep desulfurization property, Aust. J. Chem. 70 (2017) 271–279.
[69] M. Sivakumar, R. Madhu, S.-M. Chen, V. Veeramani, A. Manikandan, W.H. Hung, et al., Low-temperature chemical synthesis of $CoWO_4$ nanospheres for sensitive nonenzymatic glucose sensor, J. Phys. Chem. C 120 (2016) 17024–17028.
[70] F. Qu, N. Zhang, S. Zhang, R. Zhao, D. Yao, S. Ruan, M. Yang, Construction of $Co_3O_4/CoWO_4$ core-shell urchin-like microspheres through ion-exchange method for high-performance acetone gas sensing performance, Sensors Actuators B: Chem. 309 (2020) 127711.
[71] P. Yu, L. Wang, X. Liu, H.-G. Fu, H.-T. Yu, $CoWO_4$ nanopaticles wrapped by RGO as high capacity anode material for lithium ion batteries, Rare Met. 36 (2017) 411–417.
[72] M. Rostampour, S. Eavani, Synthesis and characterization of the novel nano composite pigments using $CoWO_4$ on different silica sources: a comparative study, Powder Technol. 2020 (363) (2020) 86–94.
[73] K. Hoang, M. Oh, Y. Choi, Electronic structure, polaron formation, and functional properties in transition-metal tungstates, RSC Adv. 2018 (8) (2018) 4191–4196.
[74] S. Rajagopal, B.V. Lv, D. Nataraj, D. Mangalaraj, O.Y. Khyzhun, Electronic structure of $FeWO_4$ and $CoWO_4$ tungstates: first-principles FP-LAPW calculations and X-ray spectroscopy studies, J. Alloys Compd. 496 (2010) 61–68.
[75] Y.L. Oliveira, M.J.S. Costa, A.C.S. Jucá, L.K.R. Silva, E. Longo, N.S. Arul, L.S. Cavalcante, Structural characterization, morphology, optical and colorimetric properties of $NiWO_4$ crystals synthesized by the co-precipitation and polymeric precursor methods, J. Mol. Struct. 1221 (2020) 128774.
[76] T.W. Swaddle, L. Fabes, Octahedral–tetrahedral equilibria in aqueous cobalt (II) solutions at high temperatures, Can. J. Chem. 58 (1980) 1418–1426.
[77] L.S. Cavalcante, J.C. Sczancoski, V.C. Albarici, J.M. Matos, J.A. Varela, E. Longo, Synthesis, characterization, structural refinement and optical absorption behavior of $PbWO_4$ powders, Mater. Sci. Eng. B 150 (2008) 18–25.
[78] M. Kakihana, Invited review "sol-gel" preparation of high temperature superconducting oxides, J. Sol-Gel Sci. Technol. 6 (1996) 7–55.
[79] A. Sen, P. Pramanik, A chemical synthetic route for the preparation of fine-grained metal tungstate powders (M = Ca Co, Ni, Cu, Zn), J. Eur. Ceram. Soc. 21 (2001) 745–750.
[80] Y. Han, K. Choi, H. Oh, C. Kim, D. Jeon, C. Lee, et al., Cobalt polyoxometalate-derived $CoWO_4$ oxygen-evolving catalysts for efficient electrochemical and photoelectrochemical water oxidation, J. Catal. 367 (2018) 212–220.
[81] CIELab. (2021). http://www.cie.co.at/.
[82] K. McLAREN, XIII-the development of the CIE 1976 (L∗ a∗ b∗) uniform colour space and colour-difference formula, J. Soc. Dyers Colour. 92 (2008) 338–341.
[83] F.A. Alharthi, H.S. Alanazi, A.A. Alsyahi, N. Ahmad, Hydrothermal synthesis, characterization and exploration of photocatalytic activities of polyoxometalate: Ni-$CoWO_4$ nanoparticles, Crystals 11 (2021) 456.
[84] H. Liu, C. Yang, W. Guo, F. Zhang, H. Lin, L. Zhao, T. Ma, X. Lu, F. Qu, $CoWO_{4-x}$-based photothermal membranes for solar-driven water evaporation and eutrophic lake water purification, ACS Omega 5 (2020) 31598–31607.
[85] M. Jeyakanthan, U. Subramanian, Enhanced DC conductivity and Seebeck coefficient of $CoWO_4/PbWO_4$ nanocomposites: role of interface, Appl. Phys. A. 127 (2021) 569.
[86] H. Weitzel, Kristallstrukturverfeinerung von Wolframiten und Columbiten, Z. Kristallogr. Cryst. Mater. 144 (1976) 238–258.
[87] S. Mourdikoudis, R.M. Pallares, N.T. Thanh, Characterization techniques for nanoparticles: comparison and complementarity upon studying nanoparticle properties, Nanoscale 10 (2018) 12871–12934.
[88] P. Debye, P. Scherrer, Interferenzen an regellos orientierten Teilcben in Röntgenlicht, Physik Z 18 (1917) 291–301.
[89] U. Holzwarth, N. Gibson, The Scherrer equation versus the 'Debye-Scherrer equation', Nat. Nanotechnol. 6 (2011) 534.
[90] C.F. Holder, R.E. Schaak, Tutorial on powder X-ray diffraction for characterizing nanoscale materials, ACS Nano 13 (2019) 7359–7365.
[91] H.M. Rietveld, Line profiles of neutron powder-diffraction peaks for structure refinement, Acta Crystallogr. 22 (1967) 151–152.
[92] H.M. Rietveld, A profile refinement method for nuclear and magnetic structures, J. Appl. Crystallogr. 2 (1969) 65–71.
[93] T.J. Ravlin, The Chebyshev Polynomials, Pure and Applied Mathematics, Wiley-Interscience, John Wiley & Sons, 1974, pp. 56–123.
[94] P. Thompson, D.E. Cox, J.B. Hastings, Rietveld refinement of Debye-Scherrer synchrotron X-ray data from Al_2O_3, J. Appl. Cryst. 20 (1987) 79–83.
[95] M. Bortolotti, L. Lutterotti, I. Lonardelli, ReX: a computer program for structural analysis using powder diffraction data, J. Appl. Cryst. 42 (2009) 538–539.
[96] H. Weitzel, H. Langhof, Verfeinerung der momentrichtungen in den magnetischen strukturen von $NiWO_4$ und $CoWO_4$, J. Magn. Magn. Mater. 4 (1977) 265–274.
[97] K. Momma, F. Izumi, VESTA: a three-dimensional visualization system for electronic and structural analysis, J. Appl. Crystallogr. 41 (2009) 653–658.
[98] K. Momma, F. Izumi, VESTA 3 for three-dimensional visualization of crystal, volumetric and morphology data, J. Appl. Crystallogr. 44 (2011) 1272–1276.
[99] R.F. Gonçalves, E. Longo, A.P. Marques, M.D. Silva, L.S. Cavalcante, I.C. Nogueira, et al., Structural investigation and photoluminescent properties of $ZnWO_4$:Dy^{3+} nanocrystals, J. Mater. Sci.: Mater. Electron. 28 (2017) 15466–15479.
[100] B. Sun, H. Li, L. Wei, P. Chen, Hydrothermal synthesis and resistive switching behaviour of $WO_3/CoWO_4$ core–shell nanowires, CrystEngComm 16 (2014) 9891–9895.
[101] J. Ruiz-Fuertes, D. Errandonea, S. López-Moreno, J. González, O. Gomis, R. Vilaplana, et al., High-pressure Raman spectroscopy and lattice-dynamics calculations on scintillating $MgWO_4$: comparison with isomorphic compounds, Phys. Rev. B 83 (2011) 214112.
[102] R. Güttinger, G. Wiprächtiger, O. Blacque, G.R. Patzke, Co/Ni-polyoxotungstate photocatalysts as precursor materials for electrocatalytic water oxidation, RSC Adv. 11 (2021) 11425–11436.
[103] R.L. Moreira, R.M. Almeida, K.P. Siqueira, C.G. Abreu, A. Dias, Optical phonon modes and infrared dielectric properties of monoclinic $CoWO_4$ microcrystals, J. Phys. D: Appl. Phys. 49 (2015) 045305.
[104] A. Kalinko, A. Kuzmin, P. Roy, R.A. Evarestov, Synchrotron-based far-infrared spectroscopy of nickel tungstate, Low Temp. Phys. 42 (2016) 552–555.
[105] C. Stella, N. Soundararajan, K. Ramachandran, Structural and optical property of $Co_{1-x}Mn_xWO_4$, AIP Conf. Proc. 1665 (2015) 050153.
[106] S. Chandrasekaran, E. Arumugam, C. Karuppiah, S. Karuppaiah, A.S. Haidyrah, B. Chandran, A novel cobalt tungstate and reduced graphene oxide composite for hydrogen evolution reaction in acid medium, Mater. Lett. 300 (2021) 130274.
[107] K. Alagumalai, M. Balamurugan, S.-M. Chen, M. Selvaganapathy, One-pot engineering of novel cashew like cobalt tungstate; dynamic electrocatalyst for the selective detection of promethazine hydrochloride, Microchem. J. 159 (2020) 105381.
[108] M. Maczka, M. Ptak, K. Hermanowicz, A. Majchrowski, A. Pikul, J. Hanuza, Lattice dynamics and temperature-dependent Raman and infrared studies of multiferroic $Mn_{0.85}Co_{0.15}WO_4$ and $Mn_{0.97}Fe_{0.03}WO_4$ crystals, Phys. Rev. B 83 (2011) 174439.
[109] C. Hess, New advances in using Raman spectroscopy for the characterization of catalysts and catalytic reactions, Chem. Soc. Rev 50 (2021) 3519–3564.
[110] L.S. Cavalcante, E. Moraes, M.A. Almeida, C.J. Dalmaschio, N.C. Batista, J.A. Varela, et al., A combined theoretical and experimental study of electronic

structure and optical properties of β–$ZnMoO_4$ microcrystals, Polyhedron 54 (2013) 13–25.
[111] J. Park, J. Joo, S. Kwon, Y. Jang, T. Hyeon, Synthesis of monodisperse spherical nanocrystals, Angew. Chem. Int. Ed. 46 (25) (2007) 4630–4660.
[112] M. Hassanpour, S.A. Tafreshi, M. Salavati-Niasari, M. Hamadanian, Toxicity evaluation and preparation of $CoWO_4$ nanoparticles towards microalga Dunaliella salina, Environ. Sci. Pollut. Res. 28 (2021) 36314–36325.
[113] X. Zhao, X. Liu, F. Yang, Q. Liu, Z. Zhang, Y. Li, Graphene oxide-supported cobalt tungstate as catalyst precursor for selective growth of single-walled carbon nanotubes, Inorg. Chem. Front. 8 (2021) 940–946.
[114] J. Wang, L. Yang, L. Zhang, Constructed 3D hierarchical micro-flowers $CoWO_4$@Bi_2WO_6 Z-scheme heterojunction catalyzer: two-channel photocatalytic H_2O_2 production and antibiotics degradation, Chem. Eng. J. 420 (2021) 127639.
[115] Y. Fan, W. Wang, J. Zhang, Y. Lu, C. Liu, S. Adimi, J. Zhou, S. Ruan, Y. Chen, Construction of *p-n* heterojunctions by modifying MOF-derived α-Fe_2O_3 with partially covered cobalt tungstate for high-performance ethyl acetate detection, Sens. Actuators. B 344 (2021) 130129.
[116] E.R. Leite, C.M. Sousa, E. Longo, J.A. Varela, Influence of polymerization on the synthesis of $SrTiO_3$: Part I. Characteristics of the polymeric precursors and their thermal decomposition, Ceram. Int. 21 (1995) 143–152.
[117] E.R. Leite, J.A. Varela, E. Longo, C.A. Paskocimas, Influence of polymerization on the synthesis of $SrTiO_3$: Part II. Particle and agglomerate morphologies, Ceram. Int. 21 (1995) 153–158.
[118] S.S. Shapiro, M.B. Wilk, An analysis of variance test for normality (complete samples), Biometrika 52 (1965) 591–611.
[119] A. Moorthy, V.R. Bellarmin, B. Kumaran, M.E. Saravanan, CTAB assisted sol-gel synthesis and characterization of $FeWO_4$ and $CoWO_4$ nanoparticles, Inorg. Nano-Metal Chem. 50 (2020) 1012–1016.
[120] S. Sagadevan, J. Podder, I. Das, Synthesis and characterization of $CoWO_4$ nanoparticles via chemical precipitation technique, J. Mater Sci: Mater Electron. 27 (2016) 9885–9890.
[121] GIMP, 2021. (s.d.). https://www.gimp.org/news/2021/05/08/gimp-2-99-6-released.
[122] P. Kubelka, F. Munk, Ein Beitrag Zur Optik Der Farbanstriche, Z. Techn. Phys. 12 (1931) 593–601.
[123] A.E. Morales, E.S. Mora, U. Pal, Use of diffuse reflectance spectroscopy for optical characterization of un-supported nanostructures, Rev. Mex. Fis. S 53 (2007) 18–22.
[124] R. Lacomba-Perales, J. Ruiz-Fuertes, D. Errandonea, D. Martínez-García, A. Segura, Optical absorption of divalent metal tungstates: correlation between the band-gap energy and the cation ionic radius, EPL (Europhysics Letters) 83 (3) (2008) 37002.
[125] M. Athar, M. Fiaz, M.A. Farid, M. Tahir, M.A. Asghar, S. ul Hassan, et al., Iron and manganese codoped cobalt tungstates $Co_{1-(x+y)}Fe_xMn_yWO_4$ as efficient photoelectrocatalysts for oxygen evolution reaction, ACS Omega 6 (2021) 7334–7341.
[126] H. Chen, D. Zheng, L. Liu, M.Y. Bartee, J. Davids, C. Macaulay, J. Strong, H. Feldmann, G. McFadden, D.A. Lomas, H.W. Virgin, A. Lucas, H_2 evolution from $H_2O/H_2O_2/MWO_4$ (M = Fe^{2+}, Co^{2+}, Ni^{2+}) systems by photocatalytic reaction, Res. Chem. Intermed. 63 (3) (2013) 252–253.
[127] X.A. López, A.F. Fuentes, M.M. Zaragoza, J.A. Guillén, J.S. Gutiérrez, A.L. Ortiz, et al., Synthesis, characterization and photocatalytic evaluation of MWO4 (M = Ni Co, Cu and Mn) tungstates, Int. J. Hydrogen Energy. 41 (2016) 23312–23317.
[128] Balasurya, S. Sv Alfarraj, L.L. Raju, A. Chinnathambi, S.A. Alharbi, A.M. Thomas et al. Novel $CoWO_4$-Ag_2MoO_4 NCs: synthesis, enhanced photocatalytic activity under visible-light irradiation and its antimicrobial activity. *Surf. Interfaces.* **2021**, *25*, 101237.
[129] P. Taneja, S. Sharma, A. Umar, S.K. Mehta, A.O. Ibhadon, S.K. Kansal, Visible-light driven photocatalytic degradation of brilliant green dye based on cobalt tungstate ($CoWO_4$) nanoparticles, Mater. Chem. Phys. 211 (2018) 335–342.
[130] M.D. Fairchild, "Color and Image Appearance Models". Color Appearance Models, 3., John Wiley & Sons, 2013, pp. 314–340.
[131] N.A. Lima, L.D.S. Alencar, M. Siu-Li, C.A.C. Feitosa, A. Mesquita, J.-C. M'peko, M. I.B. Bernardi, $NiWO_4$ powders prepared via polymeric precursor method for application as ceramic luminescent pigments, J. Adv. Ceram 9 (2020) 55–63.
[132] R. Ravindranath, A.P. Periasamy, P. Roy, Y.-W. Chen, H.-T. Chang, Smart app-based on-field colorimetric quantification of mercury via analyte-induced enhancement of the photocatalytic activity of TiO_2–Au nanospheres, Anal. Bioanal. Chem. 410 (2018) 4555–4564.
[133] J.C. Ragain, A review of color science in dentistry: colorimetry and color space, J. Dent. Oral. Disord. Ther. 4 (2016) 01–05.
[134] N. Ohta, R.A. Colorimetry, Fundamentals and Applications, John Wiley & Sons, 2005, pp. 197–204.
[135] T. Anitha, A.E. Reddy, R. Vinodh, H.-J. Kim, Y.-R. Cho, Preparation and characterization of $CoWO_4/CoMn_2O_4$ nanoflakes composites on Ni foam for electrochemical supercapacitor applications, J. Energy Storage 30 (2020) 101483.
[136] X. Li, J. Xiong, Y. Luo, Y. Luo, Electrochemical properties of RuO_2 electrodes as a function of thin film thickness, J. Electron. Mater. 47 (2018) 347–352.
[137] K. Adib, M. Rahimi-Nasrabadi, Z. Rezvani, S.M. Pourmortazavi, F. Ahmadi, H.R. Naderi, et al., Facile chemical synthesis of cobalt tungstates nanoparticles as high performance supercapacitor, J. Mater. Sci.: Mater. Electron. 27 (2016) 4541–4550.
[138] R.D. Kumar, S. Karuppuchamy, Microwave mediated synthesis of nanostructured Co-WO_3 and $CoWO_4$ for supercapacitor applications, J. Alloys Compd 674 (2016) 384–391.
[139] S. Chen, G. Yang, Y. Jia, H. Zheng, Facile synthesis of $CoWO_4$ nanosheet arrays grown on nickel foam substrates for asymmetric supercapacitors, ChemElectroChem 3 (2016) 1490–1496.
[140] K. Ding, X. Zhang, J. Li, P. Yang, X. Cheng, Formation of Dandelion-like Co_3O_4/$CoWO_4$ heterojunctions for enhanced supercapacitive performance, ChemElectroChem 4 (2017) 3011–3017.
[141] J. Ge, J. Wu, J. Dong, J. Jia, B. Ye, S. Jiang, et al., Hydrothermal synthesis of hybrid rod-like hollow $CoWO_4/Co_{1-x}S$ for high-performance supercapacitors, ChemElectroChem 5 (2018) 1047–1055.
[142] S. Sanati, Z. Rezvani, R. Abazari, Z. Hou, H. Dai, Hierarchical CuAl-layered double hydroxide/$CoWO_4$ nanocomposites with enhanced efficiency for use in supercapacitors with long cycling stability, New J. Chem. 43 (2019) 15240–15248.
[143] X. Fan, X. Chen, Hydrothermal synthesis of flower-like $CoWO_4$ with good supercapacitiveperformances. *Proceedings 11th International Conference on Nanomaterials - Research & Application*, 2019, pp. 215–220.
[144] S. Arvind, O.K.K. Animesh, Assembling $NiCo_2O_4$ nanorods to 3D layered $CoWO_4$ networks for supercapacitor electrode materials, AIP Conference Proceedings 2020 (2244) (2020) 070012.
[145] K. Thiagarajan, D. Balaji, J. Madhavan, J. Theerthagiri, S.J. Lee, K.-Y. Kwon, et al., Cost-effective synthesis of efficient $CoWO_4$/Ni nanocomposite electrode material for supercapacitor applications, Nanomaterials 10 (2020) 2195.
[146] J.-F. Hou, J.-F. Gao, L.-B. Kong, Interfacial engineering in crystalline cobalt tungstate/amorphous cobalt boride heterogeneous nanostructures for enhanced electrochemical performances, ACS Appl. Energy Mater. 3 (2020) 11470–11479.
[147] S.J. Patil, N.R. Chodankar, Y.S. Huh, Y.-K. Han, D.W. Lee, Bottom-up approach for designing cobalt tungstate nanospheres through sulfur amendment for high-performance hybrid supercapacitors, ChemSusChem 14 (2021) 1602–1611.
[148] R.B. Waghmode, H.S. Jadhav, K.G. Kanade, A.P. Torane, Morphology-controlled synthesis of $NiCo_2O_4$ nanoflowers on stainless steel substrates as high-performance supercapacitors, Mater. Sci. Energy Technol. 2 (2019) 566–574.
[149] R.B. Waghmode, H.S. Jadhav, K.G. Kanadea, A.P. Torane, Morphology-controlled synthesis of $NiCo_2O_4$ nanoflowers on stainless steel substrates as high-performance supercapacitors, Mater. Sci. Energy Technol. 3 (2021) 446–455.
[150] S.J. Uke, S.P. Mardikar, D.R. Bambole, Y. Kumar, G.N. Chaudhari. Sol-gel citrate synthesized Zn doped $MgFe_2O_4$ nanocrystals: a promising supercapacitor electrode material, *Mater. Sci. Energy Technol.* 2021, *3*, 556–564.
[151] A. Mishra, N.P. Shetti, S. Basu, K.R. Reddy, T.M. Aminabhavi, Carbon cloth-based hybrid materials as flexible electrochemical supercapacitors, ChemElectroChem 6 (2019) 5771–5786.
[152] D. Ilager, H. Seo, S.S. Kalanur, N.P. Shetti, T.M. Aminabhavi, A novel sensor based on $WO_3.0.33H_2O$ nanorods modified electrode for the detection and degradation of herbicide, carbendazim, Sci. Total Environ. 279 (2021), 111611–1–10.
[153] D. Ilager, H. Seo, N.P. Shetti, S.S. Kalanur. CTAB modified Fe-WO_3 as an electrochemical detector of amitrole by catalytic oxidation. *J. Environ. Chem. Eng.* 2020, 8, 104580-1–9.
[154] D. Ilager, H. Seo, N.P. Shetti, S.S. Kalanur, T.M. Aminabhavi, Electrocatalytic detection of herbicide, amitrole at $WO_3.0.33H_2O$ modified carbon paste electrode for environmental applications, Sci. Total Environ. 743 (2020), 140691–1–10.